

The JWST Discovery of the Triply-imaged Type Ia “Supernova H0pe” and Observations of the Galaxy Cluster PLCK G165.7+67.0

BRENDA L. FRYE,¹ MASSIMO PASCALE,² JUSTIN PIEREL,³ WENLEI CHEN,⁴ NICHOLAS FOO,⁵ REAGEN LEIMBACH,¹ NIKHIL GARUDA,¹ SETH H. COHEN,⁵ PATRICK S. KAMENESKI,⁵ ROGIER A. WINDHORST,⁵ ANTON M. KOEKEMOER,³ PAT KELLY,⁶ JAKE SUMMERS,⁵ MICHAEL ENGESSER,³ DAIZHONG LIU,⁷ LUKAS J. FURTAK,⁸ MARIA DEL CARMEN POLLETTA,⁹ KEVIN C. HARRINGTON,¹⁰ S. P. WILLNER,¹¹ JOSE M. DIEGO,¹² ROLF A. JANSEN,⁵ DAN COE,^{3,13,14} CHRISTOPHER J. CONSELICE,¹⁵ LIANG DAI,¹⁶ HERVÉ DOLE,¹⁷ JORDAN C. J. D’SILVA,^{18,19} SIMON P. DRIVER,¹⁸ NORMAN A. GROGIN,³ MADELINE A. MARSHALL,^{20,19} ASHISH K. MEENA,⁸ MARIO NONINO,²¹ RAFAEL ORTIZ III,⁵ NOR PIRZKAL,³ AARON ROBOTHAM,¹⁸ RUSSELL E. RYAN, JR.,³ LOU STROLGER,³ SCOTT TOMPKINS,⁵ CHRISTOPHER N. A. WILLMER,²² HAOJING YAN,²³ MIN S. YUN,²⁴ AND ADI ZITRIN⁸

¹Department of Astronomy/Steward Observatory, University of Arizona, 933 N. Cherry Avenue, Tucson, AZ 85721, USA

²Department of Astronomy, University of California, 501 Campbell Hall #3411, Berkeley, CA 94720, USA

³Space Telescope Science Institute, 3700 San Martin Drive, Baltimore, MD 21218, USA

⁴School of Physics and Astronomy, University of Minnesota, Minneapolis, MN 55455, USA

⁵School of Earth and Space Exploration, Arizona State University, Tempe, AZ 85287-1404, USA

⁶Minnesota Institute for Astrophysics, University of Minnesota, 116 Church St SE, Minneapolis, MN 55455, USA

⁷Max-Planck-Institut für Extraterrestrische Physik (MPE), Giessenbachstr. 1, D-85748 Garching, Germany

⁸Physics Department, Ben-Gurion University of the Negev, P. O. Box 653, Be’er-Sheva, 8410501, Israel

⁹INAF – Istituto di Astrofisica Spaziale e Fisica cosmica (IASF) Milano, Via A. Corti 12, 20133 Milan, Italy

¹⁰European Southern Observatory, Alonso de Córdova 3107, Vitacura, Casilla 19001, Santiago de Chile, Chile

¹¹Center for Astrophysics | Harvard & Smithsonian, 60 Garden Street, Cambridge, MA 02138, USA

¹²Instituto de Física de Cantabria (CSIC-C). Avda. Los Castros s/n. 39005 Santander, Spain

¹³Association of Universities for Research in Astronomy (AURA) for the European Space Agency (ESA), STScI, Baltimore, MD 21218, USA

¹⁴Center for Astrophysical Sciences, Department of Physics and Astronomy, The Johns Hopkins University, 3400 N Charles St. Baltimore, MD 21218, USA

¹⁵Jodrell Bank Centre for Astrophysics, Alan Turing Building, University of Manchester, Oxford Road, Manchester M13 9PL, UK

¹⁶Department of Physics, University of California, 366 Physics North MC 7300, Berkeley, CA. 94720, USA

¹⁷Université Paris-Saclay, CNRS, Institut d’Astrophysique Spatiale, 91405, Orsay, France

¹⁸International Centre for Radio Astronomy Research (ICRAR) and the International Space Centre (ISC), The University of Western Australia, M468, 35 Stirling Highway, Crawley, WA 6009, Australia

¹⁹ARC Centre of Excellence for All Sky Astrophysics in 3 Dimensions (ASTRO 3D), Australia

²⁰National Research Council of Canada, Herzberg Astronomy & Astrophysics Research Centre, 5071 West Saanich Road, Victoria, BC V9E 2E7, Canada

²¹INAF-Osservatorio Astronomico di Trieste, Via Bazzoni 2, 34124 Trieste, Italy

²²Steward Observatory, University of Arizona, 933 N Cherry Ave, Tucson, AZ, 85721-0009, USA

²³Department of Physics and Astronomy, University of Missouri, Columbia, MO 65211, USA

²⁴Department of Astronomy, University of Massachusetts at Amherst, Amherst, MA 01003, USA

ABSTRACT

A Type Ia supernova (SN) at $z = 1.78$ was discovered in James Webb Space Telescope Near Infrared Camera imaging of the galaxy cluster PLCK G165.7+67.0 (G165; $z = 0.35$). The SN is situated 1.5–2 kpc from its host galaxy Arc 2 and appears in three different locations as a result of gravitational lensing by G165. These data can yield a value for Hubble’s constant using time delays from this multiply-imaged SN Ia that we call “SN H0pe.” Over the entire field we identified 21 image multiplicities, confirmed five of them using Near-Infrared Spectrograph (NIRspec), and constructed a new lens model that gives a total mass within 600 kpc of $(2.6 \pm 0.3) \times 10^{14} M_{\odot}$. The photometry uncovered a galaxy overdensity at Arc 2’s redshift. NIRSpec confirmed six member galaxies, four of which surround Arc 2 with relative velocity $\lesssim 900 \text{ km s}^{-1}$ and projected physical extent $\lesssim 33 \text{ kpc}$. Arc 2 dominates the stellar mass $((5.0 \pm 0.1) \times 10^{11} M_{\odot})$, which is a factor of ten higher than other members of this compact galaxy group. These other group members have specific star formation rates (sSFR)

of $2\text{--}260\text{ Gyr}^{-1}$ derived from the $\text{H}\alpha$ -line flux corrected for stellar absorption, dust extinction, and slit losses. Another group centered on the dusty star forming galaxy Arc 1 is at $z = 2.24$. The total SFR for the Arc 1 group ($\gtrsim 400\text{ M}_\odot\text{ yr}^{-1}$) translates to a supernova rate of $\sim 1\text{ SNe yr}^{-1}$, suggesting that regular monitoring of this cluster may yield additional SNe.

Keywords: large-scale structure of universe - gravitational lensing: strong – galaxies: fundamental parameters – galaxies: clusters: general – galaxies: high-redshift

1. INTRODUCTION

The galaxy cluster PLCK G165.7+67.9 (G165; $z = 0.35$) first garnered attention by gravitationally-amplifying a single, apparently-bright galaxy in the background called “Arc 1.” Arc 1 is boosted to an observed sub-mm flux density of $S_{350\mu\text{m}} > 700\text{ mJy}$ (Cañameras et al. 2015; Harrington et al. 2016), making it detectable by the *Planck* and *Herschel Space Observatory* missions (Planck Collaboration et al. 2016, 2020a). In addition to its lensing properties, G165 also has some other unusual physical properties. It is a double-cluster with two prominent cluster cores, its X-ray luminosity is lower than galaxy clusters of a similar redshift, and its mass, based on the *Planck* SZ Compton-Y map, yields only an upper limit. These properties arise in part because the cluster has a relatively-small mass of $2\text{--}3 \times 10^{14}\text{ M}_\odot$ (Frye et al. 2019; Pascale et al. 2022), and in part because the source responsible for the high rest-frame far-infrared flux density is not the entire galaxy cluster but a only portion of a single lensed source that is a dusty and high star forming galaxy (DSFG, Casey et al. 2014) that we call herein “Arc 1 b/c.”

Strong lensing by G165 renders Arc 1 into two images merging with the critical curve, Arc 1b/c and a separate counterimage that we call herein “Arc 1a,” which together form an “image system”. The star formation rate (SFR) for Arc 1b/c uncorrected for lensing magnification was measured to be $\mu\text{SFR} \sim 12000\text{--}24000\text{ M}_\odot\text{ yr}^{-1}$ that was based on integrating the spectral energy distribution (SED) fit over a wavelength range of 8–1000 μm (Harrington et al. 2016). A requisite byproduct of this high star formation is UV radiation by massive stars. Interestingly, Arc 1b/c is detected in the rest-frame UV (observed frame g -band) (Frye et al. 2019). This is impactful because the vast majority of the light is expected to be obscured by dust (Casey et al. 2017; Whitaker et al. 2017). The UV light may be made more detectable by the high lensing magnification factor of $\gtrsim 30$ that spreads the light over more pixels, thereby potentially enabling higher signal-to-noise detections of the escaping UV radiation field. The physical conditions are less well constrained owing to the lack of a rest-frame optical spectrum with which to obtain the galaxy clas-

sification (i.e., Mingozi et al. 2023), estimate the dust extinction, investigate the star-forming properties via the Balmer emission lines (i.e., Kennicutt 1998; Shapley et al. 2022), and the measure the gas-phase oxygen abundance (i.e., Curti et al. 2020; Li et al. 2023).

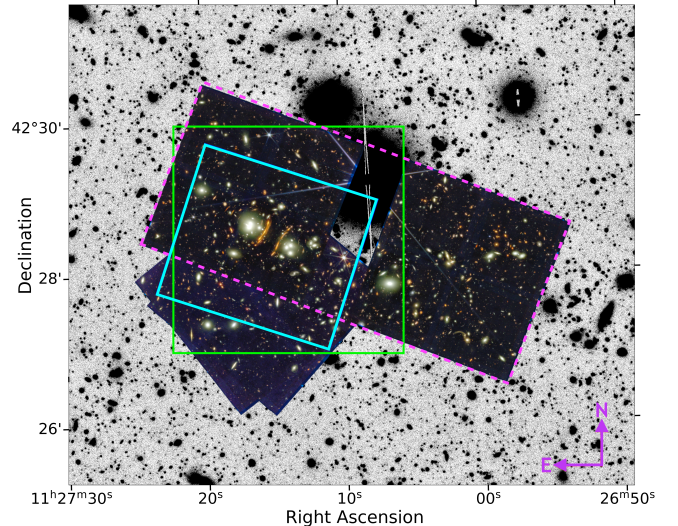


Figure 1. JWST/NIRCam coverage of the G165 field. The background is the r -band negative image from Megaprime. Color images show the combined NIRCam data. The pink long-dashed rectangle outlines Epoch 1, and Epochs 2 and 3 are squares that mostly overlap but have slightly different rotation angles. The blue square outlines the field of view of previous HST WFC3-IR imaging, which usefully covers a portion of the gap between the two NIRCam modules. The green square outlines the field of view adopted to construct the lens model.

Another prominent infrared-bright galaxy is Arc 2 ($m_K = 20.5$ AB mag), which has a robust photometric redshift based on a joint fit of the imaging from seven ground- and space-based facilities of $z = 2.30 \pm 0.32$ (Pascale et al. 2022). This redshift has recently been confirmed spectroscopically from the ground at $z_{\text{sp}} = 1.783 \pm 0.002$ (Polletta et al. 2023). Somewhat surprisingly, in Pascale et al. (2022) the photometric redshifts for several arc systems hovered around the same redshift, $z_{\text{ph}} \sim 2$. It is tempting to conclude that there is a galaxy overdensity at this redshift, but existing imaging

was inhomogeneous, with limiting magnitudes ranging from 23.3-28.9 AB and PSF point-source full-width-half-maximum values ranging from 0.13-2.02'', complicating their confirmation as $z \sim 2$ sources by their photometric redshifts alone.

HST WFC3-IR imaging enabled the identification of large sets of image systems and the construction of lens models (Cañameras et al. 2018; Frye et al. 2019). These models confirmed both the northeastern (NE) and southwestern (SW) cores of this binary cluster, and the high, cluster-scale mass. This earlier work was built and expanded upon by the addition of robust photometric redshift estimates across ground and space-based data sets for three of the 11 image systems and several cluster members (Pascale et al. 2022). Yet, these models were anchored on the spectroscopic redshift for only one image system (Arc 1), thereby limiting the accuracy of the resulting lens model and its ability to recover the lensed image positions (Johnson & Sharon 2016).

On account of its physical properties, prominently-placed infrared galaxies, and ample strong lensing evidence, G165 was observed by the James Webb Space Telescope (JWST) as a part of the Prime Extragalactic Areas for Reionization and Lensing Science (PEARLS) program (Windhorst et al. 2023). The PEARLS Near Infrared Camera (NIRCam) imaging, referred to as “Epoch 1,” uncovered three point sources which were bright ($m_{F150W} = 23.91 \pm 0.01$ AB mag) yet not present in the previous HST imaging. This triply-imaged transient was estimated to be a Type Ia supernova (SN) with at a $> 90\%$ probability based on the three points populating the light curve obtained in Epoch 1. A JWST disruptive Director’s Discretionary Time (DDT) program was executed that contained two additional imaging epochs which sum up to a total of 9 samplings of the supernova SN light curve (three per image per observing epoch). Epoch 2 imaging was scheduled three weeks after Epoch 1, so that a set of photometric points could be taken just prior to the second peak of the SN Ia light curve. Epoch 3 imaging was scheduled two weeks after Epoch 2 to bracket the second SN peak on the fading side. NIRSpec spectroscopy was obtained for all three SN appearances during Epoch 2 when they were relatively bright, and included the SN host galaxy Arc 2, and other high-priority arcs (PID: 4446, PI: Frye).

We present herein an overview of the initial science results in the combined JWST PEARLS and DDT imaging and spectroscopic observations in the G165 cluster field and of the discovery of the SN, which is dubbed “SN H0pe” for its potential to measure the time delays between the images, and from it, a value for Hubble’s constant (i.e., Kelly et al. 2023a,b; Liu et al. 2023, and

references therein). This study is the first in a series of papers whose objective is to investigate SN H0pe, the cluster, and the lensed sources.

This paper is organized as follows. §2 introduces the JWST data sets and the ancillary data. §3 describes the NIRCam photometry, the photometric discovery of SN H0pe, and the estimation of photometric redshifts. The construction of the lens model appears in §4. The NIRSpec spectroscopic analysis follows in §5 with a focus on the $z \approx 2$ galaxy groups. The physical properties of these galaxy groups are investigated in §6. §7 summarizes the results. This paper uses the AB magnitude system throughout, and we assume a flat Λ CDM cosmology with $H_0 = 67 \text{ km s}^{-1} \text{ Mpc}^{-1}$, $\Omega_{m,0} = 0.32$, and $\Omega_{\Lambda,0} = 0.68$ (Planck Collaboration et al. 2020b).

2. OBSERVATIONS AND REDUCTIONS

2.1. *NIRCam*

The Epoch 1 NIRCam observations were obtained as part of the PEARLS program (PID 1176, PI: Windhorst). The observing window was selected by STScI in order to reduce stray light expected from a nearby bright star. Exposures were taken in four filters in the short wavelength (SW) module and four in the long wavelength (LW) module as shown in Table 1. Both NIRCam modules collected data. Epochs 2 and 3 of NIRCam imaging were acquired as part of a JWST disruptive DDT program (PID 4446, PI: Frye) to follow the supernova’s light curve in each of its three images. In this follow-up program exposures were taken in six filters using only Module B of NIRCam, also recorded in Table 1. The NIRCam observations covered the central region of the cluster including both the NE and SW cluster components, the three images of the SN, the DSFG, all of the image systems, and the prominent giant arcs. Figure 1 depicts the field coverage relative to the Megaprime *r*-band image.

The images were reduced by our team as described by Windhorst et al. (2023). Briefly, the data were retrieved from the Mikulski Archive for Space Telescopes (MAST), and the latest photometric calibration files were used (pmap.1100). All images were reduced using version 1.11.2 of the STScI JWST Pipeline (Bushouse et al. 2022) with an additional correction for $1/f$ noise by applying the prescription of C. Willott¹. The ProFound code was run, which makes a second round of corrections of other image artifacts in the relevant rows and columns. This step additionally flattens the background and corrects for detector-level offsets, “wisps,”

¹ <https://github.com/chriswillott/jwst.git>

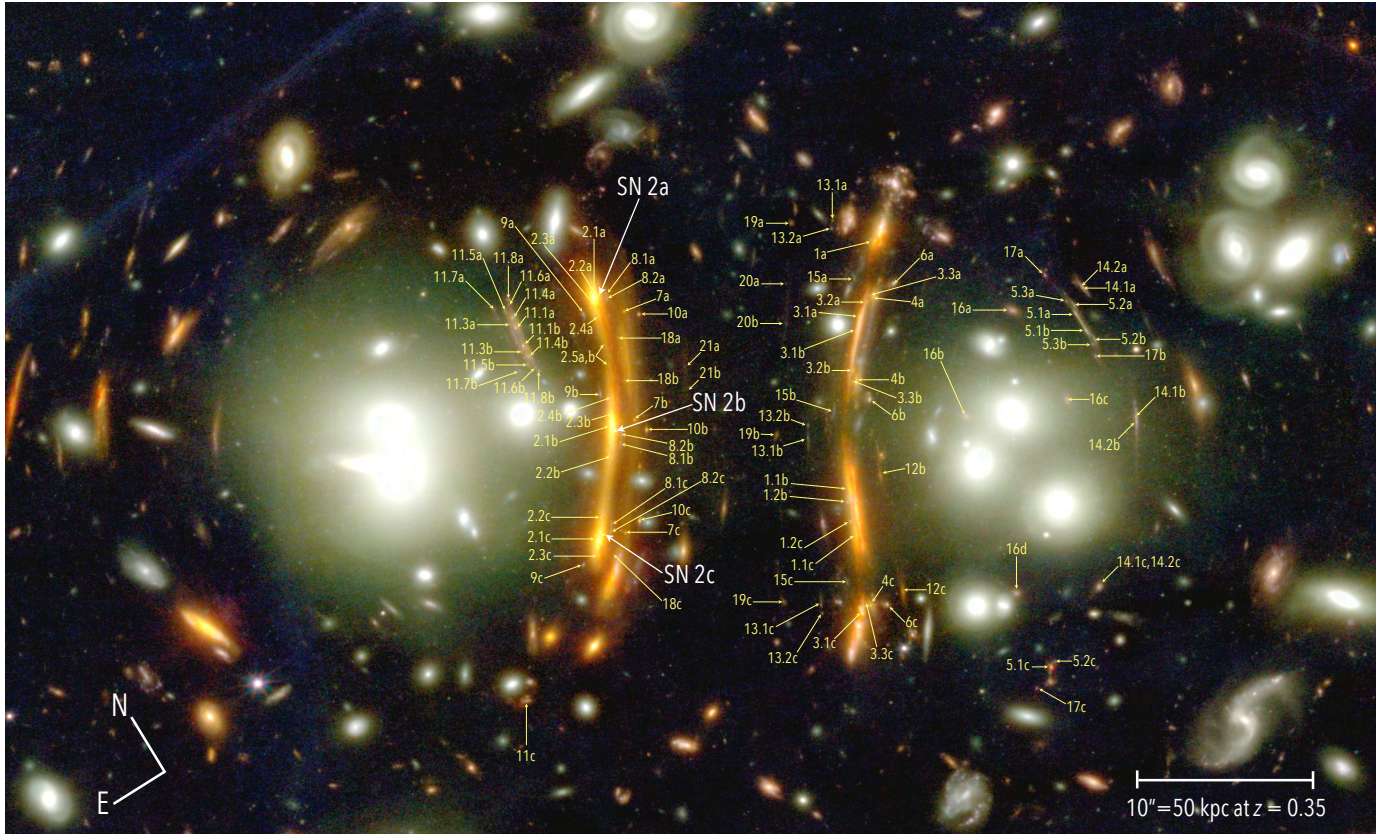


Figure 2. NIRCam color image of the central region of G165. G165 is a double cluster with prominent NE and SW components. Colors follow the prescription in Trilogy (Coe et al. 2012) with red showing F444W and F356W, green showing F277W and F200W, and blue showing F150W and F090W. The 21 image systems used in our lens model are marked. They include the DSFG as Arcs 1a and 1b/c. The triply-imaged SN is labeled as “SN 2a/2b/2c.” The orientation and image scale are provided for reference.

and “snowballs” (Robotham et al. 2017, 2018). Since the Windhorst et al. (2023) publication, improvements in the data reduction techniques have been made by Robotham et al. (2023) regarding the removal of image wisps by using the wisp-free LW images as priors to identify the outer contours of the real detected objects. Those real objects were subsequently removed from the SW images to get a pure wisp image which was then fully subtracted. This process yields an image noise in the final mosaic that is almost the same in the wisp-removed area as in the surrounding wisp-free areas.

After each frame was calibrated, the frames were aligned onto a common astrometric reference frame and drizzled into mosaics with pixel scale 20 milli-arcseconds (mas). The process was similar to that first described by Koekemoer et al. (2011) but updated to use the JWST pipeline². Mosaics were produced for each filter in each separate epoch. For the six filters in common, all epochs were combined into a grand mosaic for each filter. All

mosaics were aligned onto the same pixel grid based on deep, ground-based Megaprime images with good seeing, which had already been aligned directly onto Gaia DR3. The NIRCam data were aligned onto this grid with net offsets below 2–3 mas and no significant large-scale distortions. Figure 2 shows the central region of G165 in the main NIRCam mosaic.

2.2. NIRSpec

2.2.1. Data Reduction

NIRSpec medium-resolution Micro-Shutter Array (MSA) spectroscopy of the G165 field was obtained on 2023 Apr 22. The MSA mask was populated with the positions of the three SN appearances (SN 2a, 2b, and 2c) and two of the three images of the SN host galaxy (Arc 2a and 2c), followed by counterimages of three other image systems (Arcs 5a, 8c, and 9c). The remainder of the mask was filled with other lensed sources which summed to a total of 42 lensed targets. The observations used the grating/filter combinations G140M/F100LP to cover spectral range 0.97–1.84 μm (rest-frame 0.35–0.66 μm at $z = 1.8$)

² <https://github.com/spacetelescope/jwst>

and G235M/F170LP to cover 1.66–3.17 μm ($z = 1.8$ rest-frame 0.57–1.1 μm), both with spectral resolution $R \approx 1000$. We also acquired a PRISM/CLEAR spectrum covering 0.7–5.3 μm (rest-frame 0.25–1.9 μm) with $R \sim 20$ –300 (50–14 \AA). All of the seven supplied guide stars were acquired, resulting in especially tight pointing residuals of 1–7 mas and successful pointing even for targets near the edges of an MSA array. The science exposure times were 4420 s, 6696 s, and 919 s for G140M/F100LP, G235M/F170LP, and the PRISM/CLEAR observations, respectively. A 3-point nod pattern was selected for each observation, and each MSA slit consisted of 3 microshutters giving slit height 1.52''. MSA slits are 0''.20 wide in the dispersion direction, and the long dimension was oriented at position angle 276°.

The Stage 1 calibrated data were retrieved from MAST, and reduced using the JWST NIRSpec pipeline, version 1.11.3.³ Stage 2 and 3 reduction used the JWST pipeline with reference files “jwst_1100.pmap” for all levels of the data reduction, with an exception regarding the background subtraction, as is described below. Saturated pixels and other image artifacts were flagged in the 2D spectra. The NIRSpec IRS2 detector readout mode was used, which largely reduced the $1/f$ noise. The 2-D spectra were wavelength- and flux-calibrated based on the calibration reference data system (CRDS) context. Finally, individual calibrated 2D spectra exposures were coadded, and one-dimensional (1-D) spectra plus uncertainties were optimally extracted (Horne 1986).

The pipeline background subtraction performed well for single point sources and single small sources which were fully covered by the aperture. This is because the dithered exposures provided a good “best-fit” background consisting of the intracluster light and/or other underlying extended sources, and/or detector noise levels. Hence, the resulting NIRSpec flux from the pipeline directly gave the flux for the point/small source.

However, we lacked exposures of a separate background target/field, which made it more of a challenge to estimate the background for sources extending across multiple microshutters. One example is the SN host galaxy Arc 2 and the SN, for which all three microshutters are occupied by sources. For this case the background template formed in the NIRSpec pipeline comes from the flux through the source shutter in the dithered exposure. This “image from image” background might include some flux from the galaxy, leading to an oversubtraction of the background. A complementary problem

Table 1. JWST Epochs and NIRCam Exposure Times

Filter	Epoch 1	Epoch 2	Epoch 3
	Mar 30	Apr 22	May 09
F090W	2491	1246	1417
F115W	2491
F150W	1890	859	1246
F200W	2104	1761	1761
F277W	2104	1761	1761
F356W	1890	859	1246
F410M	2491
F444W	2491	1246	1417

NOTE—Dates of each epoch are in 2023, and exposure times for each filter are in seconds.

is the case for which neighboring microshutters are occupied by different sources. In the “MOS Optimal Spectral Extraction” tool from STScI (based on the method from Horne (1986)) a source kernel and a polynomial background template are fit at the same time for one source within an MSA slit, based on a spatial window in the 2D spectrum chosen manually by the user, but the software does not support multiple source extraction.

To alleviate some of these issues, a custom-built code was developed to perform the background subtraction. The code is different from the pipeline in that it builds a more locally-derived background template. For each pixel we evaluated the minimum flux of the set of five dithered pixels. Then for each pixel within each spatial column i the best value for the background was computed by the median value of this minimum flux within a running boxcar centered on column i that is 10 spatial columns wide. We found 10 columns to be a good compromise, for which a smaller median filter starts to encroach on the size of a typical cosmic ray mask, and a larger median filter smoothed out the background features in this wavelength-dependent operation. To cope with image crowding, the code has a multiple source extraction mode that fits multiple source kernels simultaneously for each object along the MSA slit.

Operationally, we ran NIRSpec Stage 2 with the background subtraction task turned off, and then applied the custom-built code. The detailed content of this code, and its implementation for this data set, appear elsewhere (Chen et al. 2023). The results are recorded in Table 2.

³ <https://jwst-pipeline.readthedocs.io/en/latest/index.html>

2.2.2. Spectroscopic Results

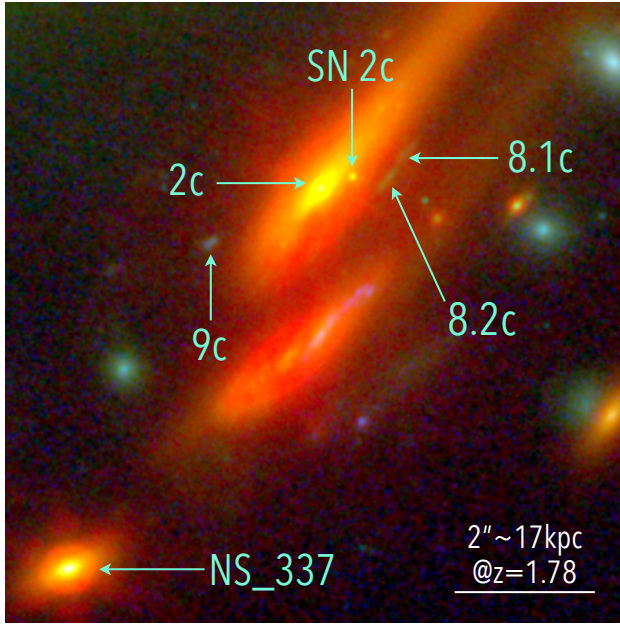


Figure 3. NIRCam color image centered on one of the SN host images 2c (Arc 2c), along with three other galaxies spectroscopically-confirmed to be at $z = 1.78$ in this study. Our lens model predicts for Arcs 2, 8, 9, and NS_337 to be situated within 33 physical kpc in the source plane. The NIRSpec spectra of these arcs appear in Figure 4. Colors follow the prescription in Trilogy (Coe et al. 2012) with red showing F444W and F356W, green showing F277W and F200W, and blue showing F150W and F090W.

In total 47 sources were extracted from the NIRSpec dataset. We measured the redshifts from emission- and absorption-line features of each source, as available. The line centers were determined by fitting Gaussians to each spectroscopic line feature using SPECUTILS (Earl et al. 2023). The 30 of 47 sources with secure measured redshifts are listed in Table 2. (A redshift is considered secure if it has a high-significance detection of two or more spectral features and $> 2\sigma$ level in the continuum.) Of these, the highest-redshift galaxy is NS_274, a relatively rare example of a quiescent galaxy at $z = 4.107$, and the highest redshift multiple image is Arc 5.1a with a redshift measured off of Balmer lines from $\text{H}\alpha$ through $\text{H}\epsilon$ detected in emission of $z = 3.9530 \pm 0.0004$. We note that the prefix “NS” stands for NIRSpec, and precedes all of the NIRSpec-confirmed galaxy images in this study.

The three SN H0pe spectra are of high quality. Most prominent is the requisite detection of the $\text{Si II } \lambda 6355$ absorption feature blueshifted to $\sim 6150 \text{ \AA}$, closely followed by the detection of the $[\text{Ca II}] \lambda\lambda 8498, 8542, 8662$ IR triplet “CaT,” amongst other spectroscopic features. The spectrum of the SN, the SN classification as Type Ia, and the measurement of the spectroscopic time de-

lay will appear in a different paper (Chen et al. 2023, in prep.). The spectra of the SN host galaxy Arcs 2a and 2b had pre-existing redshifts, both based on the joint detection of $[\text{O II}] \lambda 3727$ and the 4000 \AA and Balmer breaks (Polletta et al. 2023). The new NIRSpec spectra give the first redshift for Arc 2c, whose value matches that of Arc 2a (Table 2). Nearly 20 spectroscopic features are detected as well as the 4000 \AA and Balmer breaks. Somewhat remarkably, six different lensed sources have the same redshift as the SN. Their images are shown in Figure 3 and their spectra are presented in Figure 4. The line fluxes and equivalent widths for several absorption lines in Arc 2 are presented elsewhere (Chen et al. 2023, in prep.). This redshift is interesting because it also coincides with the strongest peak in the photometric redshift distribution after the cluster redshift, as described in § 3.3.

Arc 1b/c had a previously measured $z_{\text{sp}} = 2.2357 \pm 0.0002$ (Harrington et al. 2016). The NIRSpec spectrum (NS_969) gives the first redshift of its counterimage, Arc 1a, and the redshifts agree. A second spectrum (NS_46) in an adjacent MSA microshutter ($0''.46$ northwest) is redshifted by $\sim 1400 \text{ km s}^{-1}$ relative to Arc 1a. Both spectra, shown in Figure 5, have strong nebular emission lines and star-bursting attributes. Section 5.2 describes their nebular and stellar properties.

In some cases, most notably for Arcs 2a, 2c, and Arc NS_337, aperture losses are expected because the MSA slit coverage is smaller than the source size. To account for this shortfall, for each filter bandpass synthetic photometry was computed based on the NIRSpec PRISM spectra, which provided continuous coverage over the wavelength range of all eight NIRCam bands. We then compared our results to the NIRCam photometry integrated over the entire source. These correction factors are discussed in more detail in § 5 and have been applied to the results in Table 4, where indicated.

2.3. Other Optical and Near-infrared Observations

LBT Large Binocular Camera gi -band imaging was acquired on 2018 January 20 (2018A; PI: Frye). Images reach 3σ limiting magnitudes of 25.42 and 24.67 for g and i , respectively (Pascale et al. 2022). In the near-infrared, HST WFC3-IR exposures were taken on 2016 May 30. Images at F110W and F160W reach 3σ limiting magnitudes of 28.94 and 27.97 AB mag, respectively (Cy23, GO-14223, PI: Frye). Details of the observations, reduction, and analysis were given by Frye et al. (2019).

At longer wavelengths, LBT LUCI-ARGOS imaging was obtained in K (2016B; PI: Frye). LUCI+ARGOS

Table 2. NIRSpec Spectra

ID	R.A.	Decl.	$m_{\text{F200W,obs}}$	z_{sp}
NS_2 (SNa)	11:27:15.31	+42:28:41.02	^a	^b
NS_3 (SNb)	11:27:15.60	+42:28:33.73	^a	^b
NS_4 (SNC)	11:27:15.94	+42:28:28.90	^a	^b
NS_6 (Arc 2c)	11:27:15.98	+42:28:28.72	20.26	1.7834 ± 0.0005
NS_7 (Arc 2a)	11:27:15.34	+42:28:41.05	20.30	1.7833 ± 0.0010^c
NS_19 (Arc 5a)	11:27:13.20	+42:28:25.73	25.36	3.9530 ± 0.0004
NS_26 (Arc 8.2c)	11:27:15.89	+42:28:28.90	26.13	1.7839 ± 0.0002
NS_29 (Arc 9c)	11:27:16.11	+42:28:27.99	26.10	1.7816 ± 0.0002
NS_46	11:27:13.87	+42:28:35.67	24.04	2.2401 ± 0.0002
NS_104	11:27:00.84	+42:27:03.65	24.83	3.1109 ± 0.0004
NS_112	11:27:02.46	+42:27:10.22	21.59	0.6227 ± 0.0003
NS_123	11:27:04.64	+42:27:15.24	23.94	1.7874 ± 0.0003
NS_143	11:27:07.64	+42:27:26.22	23.28	1.6322 ± 0.0002
NS_171	11:27:05.82	+42:27:37.10	23.33	1.1787 ± 0.0002
NS_274	11:27:11.67	+42:28:10.70	23.44	4.1076 ± 0.0023
NS_285	11:27:06.82	+42:28:12.88	23.81	0.4466 ± 0.0001
NS_337	11:27:16.28	+42:28:23.59	21.77	1.7810 ± 0.0009
NS_342	11:27:19.46	+42:28:24.79	24.06	1.7664 ± 0.0009
NS_376	11:27:16.91	+42:28:30.62	22.69	0.6840 ± 0.0001
NS_407	11:27:06.62	+42:28:37.80	22.49	1.8553 ± 0.0009
NS_411	11:27:05.17	+42:28:37.75	24.28	1.2456 ± 0.0007
NS_477	11:27:04.23	+42:28:56.36	23.00	1.8524 ± 0.0009
NS_481	11:27:13.66	+42:28:57.12	24.35	1.3236 ± 0.0002
NS_505	11:27:18.95	+42:29:06.64	24.40	1.2888 ± 0.0002
NS_511	11:27:18.69	+42:29:08.42	24.13	3.3255 ± 0.0006
NS_548	11:27:13.21	+42:29:30.75	23.14	0.8161 ± 0.0003
NS_610	11:27:00.97	+42:26:48.25	22.77	0.6628 ± 0.0004
NS_969 (Arc 1a)	11:27:13.92	+42:28:35.43	24.90	2.2355 ± 0.0003
NS_1115	11:27:03.09	+42:29:07.03	23.61	2.0585 ± 0.0007
NS_1477	11:27:16.65	+42:27:23.57	21.04	0.7203 ± 0.0003

NOTE—NS numbers refer to the MSA slit identifications assigned when the observations were designed. Positions are object positions as measured on NIRCam images.

^aThe photometry will be presented by Pierel et al. (2023, in prep.)

^bThis spectroscopic redshift will be presented by Chen et al. (2023, in prep.)

^cThe spectroscopic redshift for this arc was first measured by Polletta et al. (2023).

corrects the atmosphere for ground-layer distortions via multiple artificial stars that are projected by laser beams mounted on each of the two 8.4 m apertures (Rabien et al. 2019). This imaging achieves a mean point-source FWHM of 0''.29 but a limiting magnitude of only 24.07 (Frye et al. 2019). And finally, Spitzer Space Telescope/Infrared Array Camera (IRAC) 3.6 and 4.5 μm images were acquired in 2017 (Cy 13, PID 13024, PI: Yan). The HST, LBT LUCI+ARGOS K -band observations, and the Spitzer observations provide baseline imaging prior to the SN event but otherwise are super-

sed by the deeper and higher-resolution NIRCam images.

Spectroscopy of G165 was acquired using LBT/LUCI long-slit during Director’s Discretionary Time on 2023 Apr 16 (PI: M. Nonino) to measure the redshift of the SN host galaxy Arc 2. The 240''-long slit was aligned along two of the three images of this triply-imaged galaxy: Arcs 2a and 2b. The data were acquired using the G200 grating with the zJspec filter to cover wavelengths 0.95–1.37 μm . The observations were carried out in binocular mode resulting into a total exposure time of 6 hours. The data reduction and analysis were presented

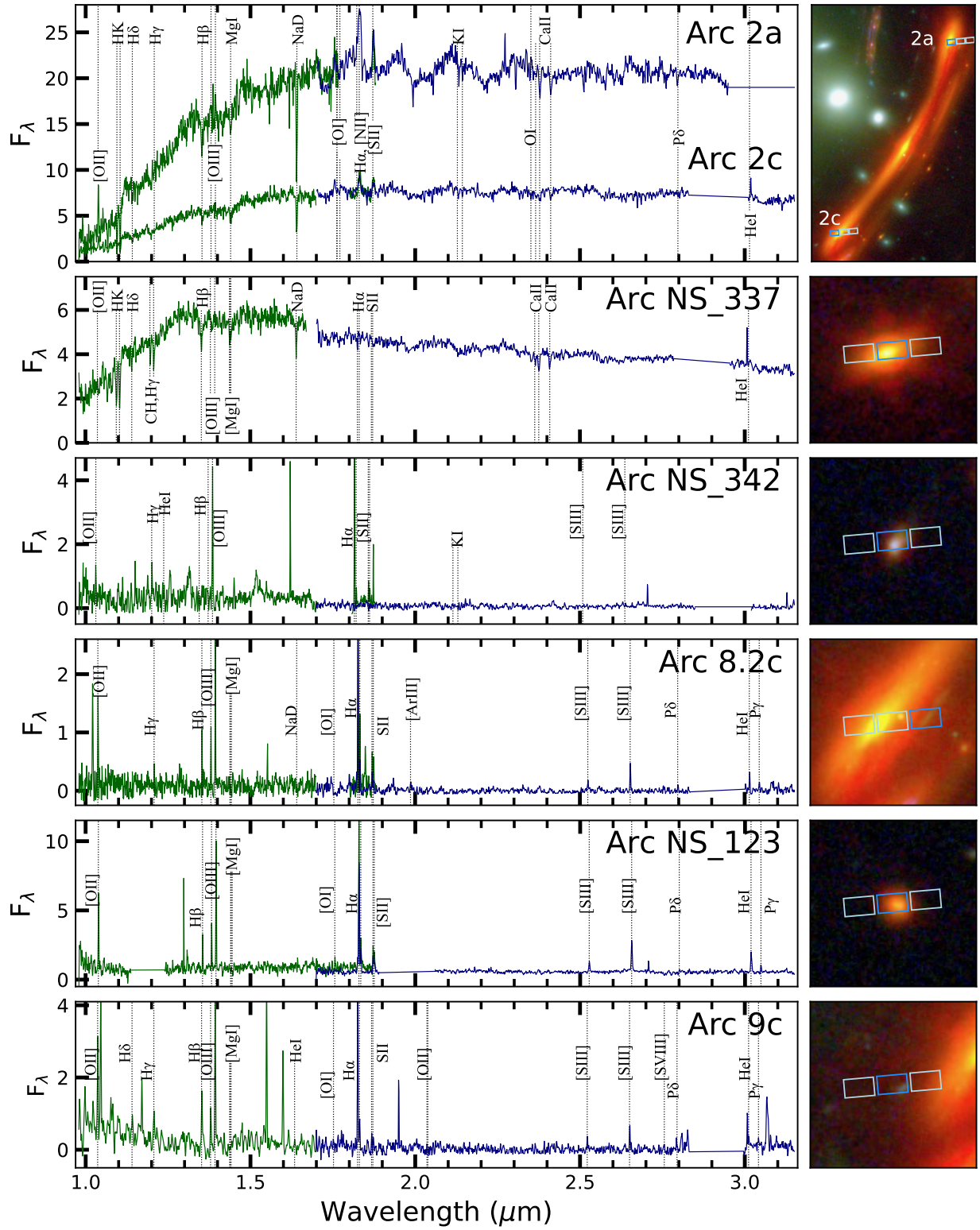


Figure 4. NIRSpec spectra of lensed sources at $z \approx 1.78$. Wavelengths are in the observed frame, and the ordinate shows F_λ in units of $10^{-19} \text{ erg s}^{-1} \text{ cm}^{-2} \text{ \AA}^{-1}$. The G140M spectrum is plotted in green and the G235M spectrum in blue. Detected lines are marked. The images to the right of each panel show the respective source with MSA slit positions overlaid and are oriented the same as in Figure 1. Colors follow the prescription in Trilogy (Coe et al. 2012) with red showing F444W and F356W, green showing F277W and F200W, and blue showing F150W and F090W. The microshutter depicted in blue is the one from which the spectrum was extracted. The spectra are presented in order of star formation activity with more quiescent sources with weaker H α emission lines and stronger 4000 \AA and Balmer breaks at the top to emission-line sources with multiple nebular emission lines at the bottom. These six sources uncover a diverse set of galaxy properties all contained in this single high-redshift galaxy overdensity. The spectrum for Arc G165.2a appears brighter and redder than the one for Arc G165.2c owing to the slit being better centered on the source.

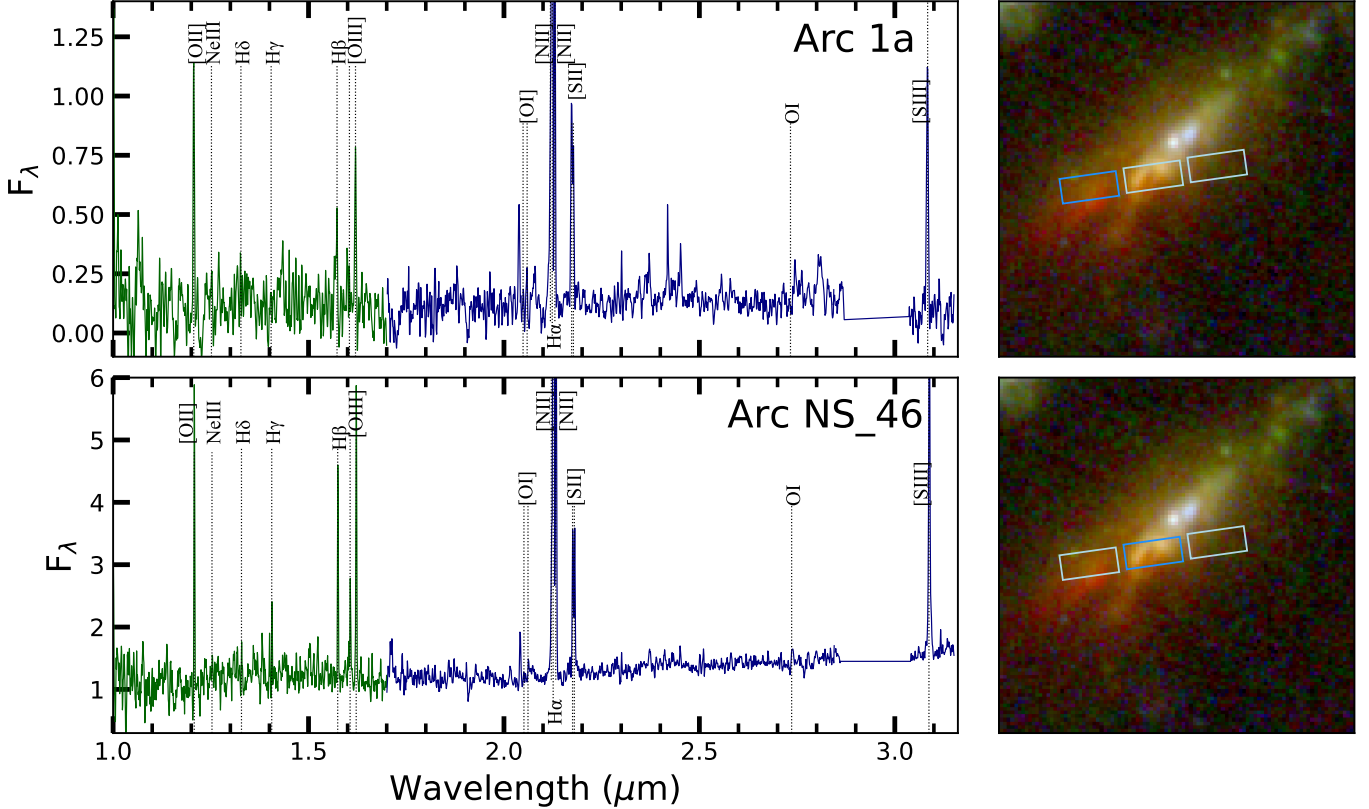


Figure 5. NIRSpec spectra of Arc 1a (=Arc NS_969, top) and a nearby object (Arc NS_46, bottom). Wavelengths are in the observed frame, and the spectra are in F_λ in units of $10^{-19} \text{ ergs}^{-1} \text{ cm}^{-2} \text{ \AA}^{-1}$. The G140M spectrum is plotted in green and the G235M spectrum in blue. Detected lines are marked. The images to the right of each panel show the respective source with MSA slit positions overlaid, and are oriented the same as in Figure 1. Colors follow the prescription in Trilogy (Coe et al. 2012) with red showing F200W, green showing F150W, and blue showing F090W. The objects were observed in the same triplet of MSA slits with Arc 1a in the easternmost segment and Arc NS_46 in the middle segment, neither perfectly centered in the respective segments. The blue outline in each image shows the microshutter from which the spectrum to its left was extracted.

by Polletta et al. (2023). The spectra for Arc 2a and 2b both show stellar continuum, the 4000 Å and Balmer breaks, and the [O II]λ3727 emission line. These give the SN host redshift $z = 1.783 \pm 0.002$ (Polletta et al. 2023). The redshifts of a few lower redshift galaxies intercepted by the long-slit were also measured which do not match the cluster redshift or that of any known image system and will appear in a different paper.

MMT/Binospec long-slit spectroscopy was obtained in Director’s Discretionary Time on 2023 Apr 18 (PI: Willner) to measure the redshift of the brightest cluster galaxy (BCG) in the entire field, which resides in the northeast (NE) cluster component. The slit position angle 118°.5 was selected to intercept the BCG and another cluster member in the southwest component that lacked a spectroscopic redshift. The data were acquired with the G270 grating to provide wavelength coverage from 3800 to 9200 Å. The total science exposure time was 1800 s. The observing conditions were good and reasonably stable, with atmospheric seeing ranging from 1''.17–1''.25.

The data were reduced using the observatory pipeline, which performed the usual calibrations (bias correction, flat-fielding, wavelength calibration and relative flux correction), as well as the coaddition of the three separate 600s exposures and extraction of the 1-D spectra⁴. Although redshift-fitting software was available, we opted to measure the spectroscopic redshifts using our own software that contains a library of spectroscopic features and a reference sky spectrum extracted from the pre-sky-subtracted data. A redshift was measured for the BCG of $z = 0.3368$. This redshift and others intercepted by the long-slit appear in Table 3.

In all, the spectroscopy includes the following new contributions: 30 redshifts equating to 28 nonredundant individual sources (NIRSpec), 2 redshifts equating to 1 individual source (LBT/LUCI), and 6 redshifts corresponding to 5 nonredundant sources (MMT/Binospec). The total sums up to 35 new redshifts. When combined

⁴ https://bitbucket.org/chil_sai/binospec

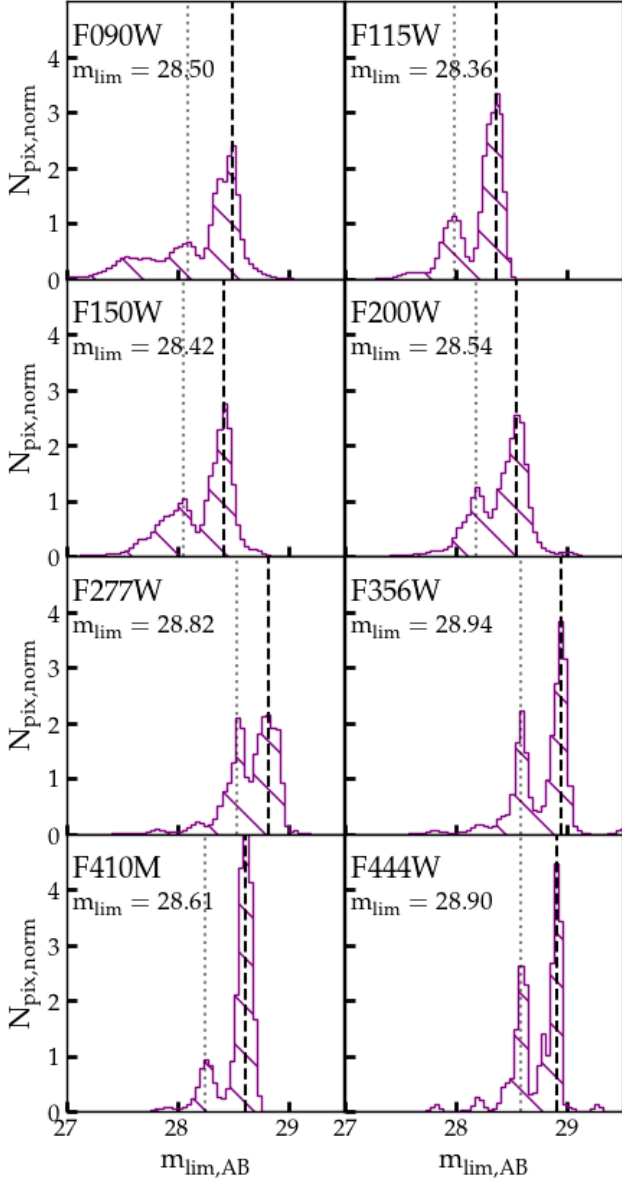


Figure 6. Limiting magnitudes (5σ) within a $0.^{\prime\prime}2$ aperture based on the corrected RMS maps (§3.1). The dashed vertical lines mark the mode of each distribution, and values are given in each panel’s label. The dotted line marks the shallower peak, corresponding to the non-overlapping regions of Epochs 2 and 3. The deeper peak corresponds to the non-overlapping regions of the Epoch 1 images, however the dithering causes the edges of the Epoch 1 images to contribute to the lower peak due to the lower exposure time in those regions. The tail of the deeper peak towards still fainter magnitudes results from the combination of the three epochs of imaging. It is not present in the F115W and F410M filters, which were acquired only in Epoch 1.

with redshifts from the literature (Frye et al. 2019; Pascale et al. 2022), the spectroscopic catalog contains 175 redshifts. Of these, 34 fall within $\pm 4000 \text{ km s}^{-1}$ of the

cluster mean redshift $z = 0.348$, and we consider these to be confirmed cluster members. Interestingly, there is a lack of detection of a relative velocity difference between the NE and SW cluster components, implying a configuration oriented preferentially in the plane of the sky (Frye et al. 2019; Pascale et al. 2022).

3. IMAGING RESULTS

3.1. *NIRCam* Photometry

The extraction of multi-band photometry broadly follows the approaches of Merlin et al. (2022) and Paris et al. (2023), which balance the need to make faint image detections while also limiting the introduction of spurious sources. Initial source detection was performed using SExtractor (Bertin & Arnouts 1996) in a two-step HOT+COLD process similar to Galametz et al. (2013). The JWST NIRCam F200W image was assigned as the reference image, which corresponds to the diffraction limit of the telescope. For severely blended objects, a separate catalog using F090W for detection was introduced owing to the sharper PSF.

The object fluxes and uncertainties were measured in each filter using APHOT (Merlin et al. 2019) by assigning Kron-like elliptical apertures, isophotal apertures, and circular apertures of diameter $0.^{\prime\prime}3$. To compute realistic photometric uncertainties, 5000 point sources from WebbPSF (Perrin et al. 2015) of known fluxes were injected into blank regions of the images, and fluxes and uncertainties were estimated using $0.^{\prime\prime}1$ apertures using APHOT with the RMS maps associated with the images. The RMS maps were then rescaled such that the RMS of the measured flux distribution was consistent with the values expected from APHOT. Because the mosaic was drizzled from 3 separate pointings, this analysis was performed separately on each overlapping and non-overlapping region between the 3 epochs of data.

The final photometry is PSF-matched using PSF models generated from WebbPSF, where all filters are degraded to the PSF of the F444W image using `pypher`. The F444W image is chosen because it has the largest PSF. The PSF models provided satisfactory convolution kernels and are found to ameliorate the trend for the F200W – F444W colors to be bluer than their true values for multi-exposure image mosaics simulated for the CEERS project (Bagley et al. 2022). We refer to (Pascale et al. 2022) for details regarding its implementation.

The histograms of the limiting magnitudes were computed separately and are shown for each filter in Figure 6. The double-peaked distributions demonstrate the multi-epoch experimental setup, with the PEARLS (Epoch 1) being deeper, and so showing a peak at

Table 3. MMT/Binospec Spectroscopy

ID	R.A.	Decl.	m_{obs}^a	z_{sp}
BCG	11:27:16.70	+42:28:38.75	17.69	0.3368
s101	11:27:14.05	+42:28:21.12	18.81	0.3427
s102	11:27:08.04	+42:27:44.95	21.52	0.2757
s103	11:27:20.51	+42:29:02.01	22.14	0.4135
s104	11:27:35.83	+42:30:33.25	^b	0.2300
s105	11:27:32.70	+42:30:14.07	^b	0.3509

NOTE—The object identifications (IDs) are arbitrary and used only for convenience in this paper. Positions are object positions as measured on NIRCam images.

^aThe AB magnitude is measured in the F090W filter that most overlaps with the MMT/Binospec spectroscopic coverage.

^bSource is outside the field of view of the JWST PEARLS program.

higher limiting magnitudes per pixel. The tail of the Epoch 1 peak towards fainter magnitude emerges from the combination of all three epochs and is not present in the F115W and F410M filters, which have coverage only in Epoch 1. The data are shallowest in F115W ($m_{lim,AB} = 28.34$) and are deeper in all of the LW filters relative to the SW filters.

3.2. SN H0pe

Three new point-source images were identified in the Epoch 1 imaging close in projected proximity to Arc 2, and with an source plane separation estimated from our lens model of 1.5–2 kpc. The geometrical arrangement of the point source relative to the arc flips parity on crossing the critical curve between images Arc 2a and Arc 2b and again between the Arc 2b and Arc 2c images, as predicted by lensing theory if the point source is associated with Arc 2. Since the point source follows the same lensing geometry as Arc 2 it is not a spurious source or low-redshift interloper, and so is likely at the same redshift as Arc 2. The triply imaged point source was easily bright enough ($m_{F150W,AB} = 23.91$ mag) to have been detected in the earlier HST imaging had the source been present in 2016 (Figure 7). The geometry and transient behavior immediately suggested a supernova in the Arc 2 galaxy, and this was confirmed by later observations as detailed below. For this paper, the three images (Figure 7) are referred to as SN 2a, 2b, and 2c, and we refer to §4 for a description of our lens model.

Figure 8 shows the photometry from the Epoch 1 imaging, with the reddest filters (F356W, F444W) removed due to contamination from the host galaxy. The

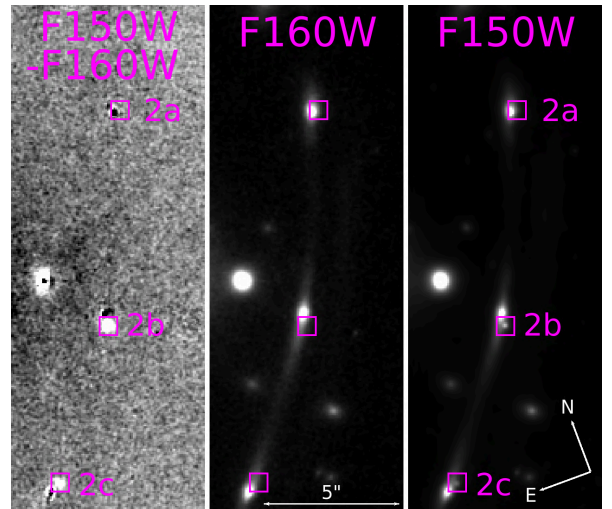


Figure 7. Residual image (left panel) after subtracting HST/WFC3 F160W (middle panel) from JWST NIRCam F150W (right panel, degraded to match the F160W PSF). This subtraction led to the serendipitous discovery of SN H0pe in all three images of Arc 2. Arc 2b is brightest, followed by 2c and then 2a. The image order based on the predicted time delay from the lens model is 2a, 2c, and then 2b. The HST/WFC3 imaging was obtained on 2016 May 30, and the JWST NIRCam PEARLS imaging was obtained on 2023 March 30.

light curve was applied only to the Epoch 1 photometry. The best-fit is for a Type Ia SN, where the light curve template was drawn from Hsiao et al. (2007). This classification predicts a second peak, which for $z = 1.78$ will appear at observed wavelengths $\gtrsim 1.8\mu\text{m}$. The lens model predicts that the SN 2a image arrived first, and this image is faint in Epoch 1, potentially intercepted already following the the second peak. The model predicts SN 2c should be the second image followed by SN 2b, which apparently was at or very near the first peak. The light curve points, although sparse, were additionally best fit by a Type Ia SN model with $>90\%$ probability, using the photometric light curve classifier from Rodney et al. (2014). These initial light curve fits are only approximations, and so are not useful for estimating the time delay. At the same time, they were sufficiently compelling to have Epochs 2 and 3 approved and executed in our disruptive DDT program.

The photometry and spectroscopy in Epochs 2 and 3 confirmed the Type Ia SN designation. The imaging in three representative filters that covers all three epochs is shown in Figure 9. As expected based on the lensing predictions, SN 2a is brightest in Epoch 1 in all filters and fades thereafter. SN 2b is the last image to arrive. It is relatively bright in all three epochs because all three are near its light-curve peak. SN 2c is the intermediate image, which is seen after the first

peak even during Epoch 1. Accordingly this image fades in bluer filters but remains bright especially in the LW filters. The full photometry, the methods for performing the photometry corrected for background galaxy halo light and microlensing effects, and the photometric time-delay measurements, are presented by Pierel et al. (2023, in prep.). The supernova spectra, the SN type classification, and the spectroscopic time-delay measurement are presented in Chen et al. (2023, in prep.).

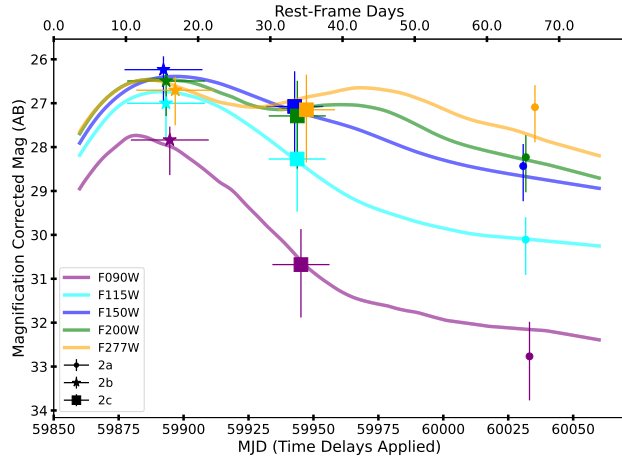


Figure 8. Photometry for SN H0pe based on Epoch 1 imaging. The abscissas are in observed frame (lower) and rest-frame (upper), where the observation epoch was MJD = 60033. The three images gave photometry for the three different times sampled, with SN 2b arriving first (corresponding to MJD = 60033), followed by SN 2c, and then SN 2a, as indicated in the legend. Each point is further corrected for lensing magnification and time delays according to the best-fit lens model (§4). Points are slightly offset horizontally for clarity (such as for the F277W filter), and lines show best-fit model light curves color-coded by filter as indicated.

3.3. Photometric Redshift Estimates

Estimates of the photometric redshifts z_{ph} were made across the grand mosaic using EAZY (Brammer et al. 2008; Brammer 2021) and LePhare (Arnouts & Ilbert 2011). EAZY spectral energy distribution (SED) templates were optimized for the identification of high-redshift galaxies in JWST/NIRCam imaging (Larson et al. 2022). A comparison of the 63 galaxies which have both spectroscopic and photometric redshifts shows good agreement for both approaches. In 95 % of cases, the photometric redshifts are within 15 % of the spectroscopic redshifts. We briefly examine the only three outliers present across the two codes (Figure 10). The one source with a photometric redshift that is too high $z_{ph} \sim 6.3 - 6.4$ compared to the spectroscopic redshift $z_{sp} = 1.13$ has a secondary redshift solution at $z_{ph} = 1.5$ with a nearly equivalent goodness of fit.

Of the two outliers with lower than expected photometric redshifts, one is found by LePhare at $z_{ph} = 0.5$ with $z_{sp} = 3.95$, and one found by EAZY at $z_{ph} = 0.08$ with $z_{sp} = 3.3$. The LePhare outlier is Arc 5.1a, which has a less favored secondary solution at $z_{ph} \sim 4.1$, a degeneracy which may be common at this redshift (Frye et al. 2023). The EAZY outlier has filter fluxes significantly enhanced by emission lines, LePhare’s treatment of which is typically found to perform better, on average (Adams et al. 2023; Frye et al. 2023).

Following this test of our photometric redshift approach, we then extended the photometric redshift estimates to the full multi-band object catalog. A photometric redshift is considered secure if the object is: (1) in the field-of-view for all filters, (2) detected in a minimum of six filters, and (3) spatially resolved from its neighbors. The resulting distribution of photometric redshifts peaks at the cluster redshift and displays minor peaks at the $z \approx 1.7$ and $z \approx 2.3$ bins (Figure 10). The $z = 1.7$ bin corresponds to the redshift of the SN, providing evidence that the SN host galaxy (Arc 2) may be one member of a larger galaxy group. Meanwhile, the peak at $z = 2.3$ aligns with the redshift of the lensed DSFG Arc 1, from which we infer that Arc 1 may be part of another background galaxy group. The physical properties of these two groups are discussed in §6.2.

4. STRONG LENSING MODEL

4.1. Lens Model Constraints

The light-traces-mass (LTM) model requires as inputs the positions and masses of cluster members, the cluster redshift, and the image systems’ identities, positions, and redshifts if known. We selected cluster members by their spectroscopic redshifts, when available, and augmented this list with sources selected by their near-infrared colors. In particular, the “ $1.6 \mu\text{m}$ bump” is a feature of the stellar populations of $\gtrsim 1$ Gyr galaxies, appearing when massive stars no longer dominate the composite galaxy emission spectrum (Sawicki 2002). For a cluster at $z = 0.35$, the $1.6 \mu\text{m}$ bump appears as a positive slope in the F090W – F150W color and a negative slope in the F277W – F444W color. Figure 11 shows the color–color selection for G165: $\text{F090W} - \text{F150W} > 0.5$ and $\text{F277W} - \text{F444W} < -0.5$. The galaxies with spectroscopic redshifts reassuringly occupy the expected region of this color–color space. The cluster list is also in agreement with the “red cluster sequence” method for identifying cluster members (Gladders & Yee 2000), and enables longer-wavelength selection. The one outlier at $\text{F090W} - \text{F150W} = 0.35$ and $\text{F277W} - \text{F444W} = -0.43$ has $z = 0.3548$ that places it in the cluster, but this galaxy’s photometry was skewed by nebular emission

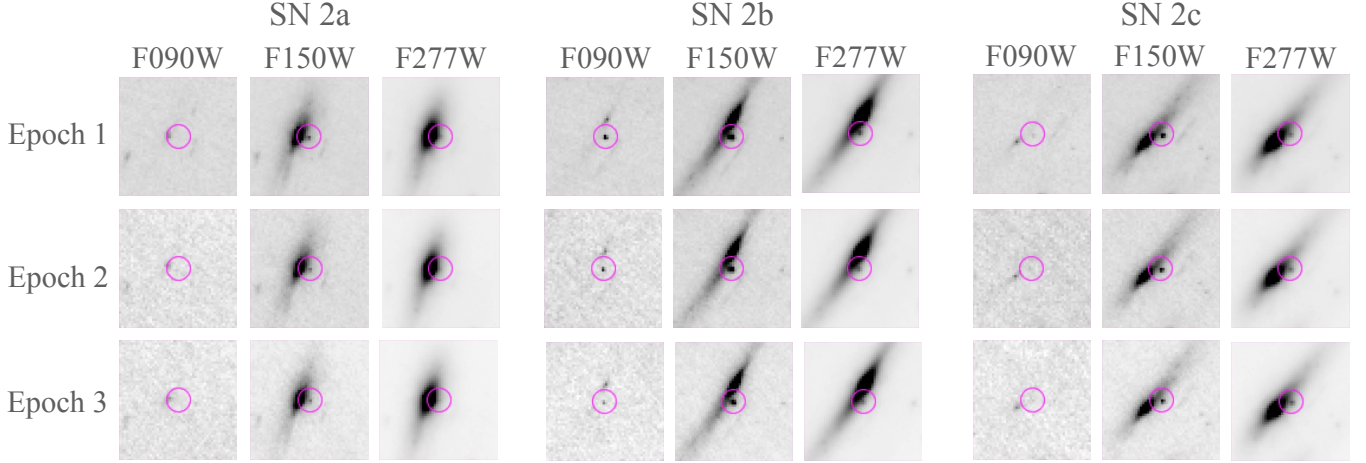


Figure 9. Time series of SN H0pe imaging observations. Negative images in the three epochs are shown for each of the three images of the SN. Of the eight NIRCam filters acquired in Epoch 1 and six filters in each of Epochs 2 and 3, only three filters are depicted for clarity. The image stamps have the same orientation as in Figure 1 and are $3''$ on a side. The SN appeared first in image 2a, where it was intercepted on the decline after the second IR peak in the light curve. SN 2a and SN 2b were intercepted near the first peak, and Epochs 2 and 3 also trace the second peak detected in the NIRCam LW channels of this Type Ia SN.

lines. The main catalog of cluster members contains 161 galaxies enclosed in a region of $3'$ on a side centered on (R.A., Decl.) = (11:27:13.9143, +42:28:28.427) and depicted by the large green square in Figure 1.

The initial lensing constraints include the 161 cluster members and the 11 known image systems (Frye et al. 2019). New spectroscopic redshifts from NIRSpec increased the value of Arcs 5, 8, and 9 as lensing constraints. A new lens model was then constructed and used to identify new image systems. Table A1 gives the complete list of image systems.

4.2. Light-traces-mass Model

The LTM modeling approach is fast and allows for the straightforward incorporation of lensing evidence and especially of the image multiplicities (Broadhurst et al. 2005; Zitrin et al. 2015). The model presented in this study is the first NIRCam-based lens model, and builds and expands upon this previous work. We refer to Frye et al. (2019) and Pascale et al. (2022) for details regarding the construction and implementation of the LTM model in the G165 field. The base model for this study included the 11 known image systems as lensing constraints. It also included the 161 cluster members identified above, which were each assigned a mass proportional to the galaxy’s luminosity with the mass-to-light ratio being a free parameter determined by the model.

Starting with this base model, the redshifts for systems 1, 2, 5, 8, and 9 were fixed at their spectroscopic values while allowing the parameters of the remaining image systems free to be fit by the model. Additional image systems were then introduced gradually, each

time making sure that the fit improved. This process identified 10 new image systems which we apply as lensing constraints and which are reported in Table A1. For image systems with multiple components, we separated spatially resolved individual clumps, as recorded in the table. This is because the relative locations of individual clumps within an image provided additional constraints on the lens model. We stopped including these minor constraints when the χ^2 -square did not indicate an improvement in the overall fit.

Figure 12 shows the model for which χ^2 is minimized. This model reproduces the angular positions of input lensed images to an RMS difference of $0''.65$. We note that while this uncertainty in predicting counterimage positions seems large compared to the NIRCam pixel size, it is not due to NIRCam WCS errors. Instead is due to the inability of the lens model to precisely locate all the lensing mass at the right locations in the model. Yet, the stated RMS is generally accurate enough to identify all the plausible counter images, and hence to refine the lens model. Based on our lens model, the lensing mass within (projected) 600 kpc of the cluster’s luminosity-weighted center is $(2.6 \pm 0.30) \times 10^{14} M_{\odot}$ with the uncertainties computed by following the approach of (Pascale et al. 2022). This value is consistent with the masses estimated by Pascale et al. (2022) and by Frye et al. (2019) to within the uncertainties.

5. SPECTROSCOPIC ANALYSIS OF THE ARC 1 AND ARC 2 GALAXY GROUPS

5.1. Diagnostic Tools

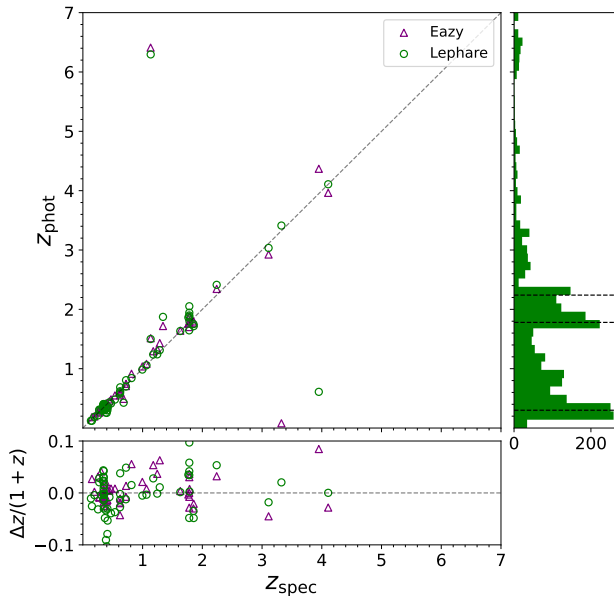


Figure 10. Photometric vs. spectroscopic redshifts. Points depict EAZY and LePhare redshifts as indicated in the legend. The panel on the right gives the histogram of photometric redshifts using LePhare, which peaks first at the G165 cluster redshift and then again at the redshift of the SN of 1.78 and at the redshift of the DSFG (indicated by the dashed lines). Bottom panel shows $|\delta z|/(1+z)$ directly.

The NIRSpec spectra and NIRCam photometry are modeled simultaneously to provide galaxy physical properties and star forming activity levels. Modeling is based on FAST++ (Schreiber et al. 2018; Kriek et al. 2009).⁵ This SED-fitting code incorporated the NIRCam photometry and all of the NIRSpec spectroscopic information (the G140M, G235M, and PRISM data), thereby accounting automatically for any strong emission-line features, which may not be apparent in the photometry alone. Models are based on a single burst with a range of decay rates τ and a star formation rate $SFR(t) \propto \exp(-t/\tau)$, where t is the time since the onset of star formation. The models that provide good fits to the JWST data return information relevant to this study such as the underlying stellar absorption, the dust extinction, and the stellar mass. For galaxies without Balmer emission lines, the dust extinction A_V was extracted from the FAST++ SED fit, and $E(B-V)$ was computed based on the Calzetti et al. (2000) reddening law.

Emission lines provide diagnostics on the galaxy classification and activity levels (Baldwin et al. 1981; Curti et al. 2020, 2023; Li et al. 2023; Mingozi et al.

2023, and references therein). The accessible emission lines are $[\text{O II}] \lambda 3727$, $\text{H}\beta$, $[\text{O III}] \lambda\lambda 4959, 5007$, $\text{H}\alpha$, $[\text{N II}] \lambda\lambda 6548, 6584$, and $[\text{S II}] \lambda\lambda 6717, 6731$. We used SPECUTILS to measure the line fluxes of $\text{H}\alpha$, $\text{H}\beta$, and other lines directly from the continuum-subtracted spectrum or via multiple-line fits when $\text{H}\alpha$ is blended with $[\text{N II}] \lambda 6584$. These two line fluxes were corrected for underlying stellar absorption based on FAST++ estimates. Typical values for these equivalent width corrections were $\sim 2 \text{ \AA}$ for $\text{H}\alpha$ and $< 4 \text{ \AA}$ for $\text{H}\beta$, both being in the expected ranges (Reddy et al. 2018; Sanders et al. 2021). The $\text{H}\alpha$ line flux was then corrected for dust extinction based on the measured Balmer decrement (e.g., Domínguez et al. 2013). For $\text{H}\alpha$ and $\text{H}\delta$ and for the computation of $D(4000)$ we followed the Balogh et al. (1999) definitions. Otherwise, the line fluxes and equivalent widths typically were measured over a $\sim 1000 \text{ km s}^{-1}$ width centered on the line core. Given the grating dispersion of 6.4 \AA pix^{-1} , this amounts to ~ 8 pixels. Decreasing this velocity width often resulted in a loss of signal near the line tails. This study follows the usual convention that negative equivalent widths indicate emission, and positive values indicate absorption, but exceptions are that $\text{H}\alpha$ and $[\text{O II}] \lambda 3727$ in emission are expressed as positive numbers.

For galaxies that show strong emission lines, the $\text{H}\alpha$ line flux and Balmer decrement give SFR and dust extinction (A_V) directly. Other emission lines constrain the galaxy activity levels. The emission-line ratios $[\text{O III}]/\text{H}\beta$ (R_3), $[\text{N II}]/\text{H}\alpha$ (N_2), $[\text{S II}]/\text{H}\alpha$ (S_2), and $[\text{O I}]/\text{H}\alpha$ place the galaxy with respect to the Kewley et al. (2006) maximum-starburst line that separates star-forming galaxies (SFGs) from active galactic nuclei (AGNs) (e.g., Mingozi et al. 2023). The above line ratios plus $([\text{O III}]5007/\text{H}\beta)/([\text{N II}]6584/\text{H}\alpha)$ (O_3N_2), $([\text{S II}]6716, 6730/\text{H}\alpha) + ([\text{O III}]5007/\text{H}\beta)$ (RS_{32}), and $([\text{O III}]5007/\text{H}\beta)/([\text{S II}]6716, 6730/\text{H}\alpha)$ (O_3S_2) allow multiple estimates of the gas-phase metallicity.

In some cases the MSA slit does not fully cover the source galaxy’s light, making the measured line fluxes lower limits. To compute a correction factor for incomplete coverage of the lensed sources, we performed photometry using the PRISM spectra, which provided uninterrupted coverage of all 8 NIRCam bands. This synthetic photometry is then compared with the NIRCam photometry, with the errors coming from the standard deviation of the differences between the 8 synthetic photometric values from their true photometric values. This correction factor was then applied to the values in Table 4, where stated. On applying the corrections for underlying stellar absorption, dust extinction, and incomplete slit coverage of the source, the $\text{H}\alpha$ flux was used to

⁵ <https://github.com/cschrreib/fastpp>

derive the SFR using the Kennicutt (1998) relation. The specific star formation rate (sSFR) was then computed by dividing the measured SFR by the stellar mass from FAST++. We note that this correction for incomplete slit coverage of the source are applied to the SFR but not to the stellar mass. This is because the stellar mass is computed by the SED fit scaled to the photometry integrated over the entire source. The uncertainties on the line fluxes and SFRs stem from the stated uncertainties of the flux values propagated by bootstrapping with a minimum of 100 realizations with the standard deviation of the distribution yielding the uncertainties. We proceed to investigate the physical properties of the Arc 1 and Arc 2 systems by a spectroscopic analysis. A more detailed spectroscopic line analysis that includes also radio information will appear in an upcoming paper (Foo et al. 2023, in prep.).

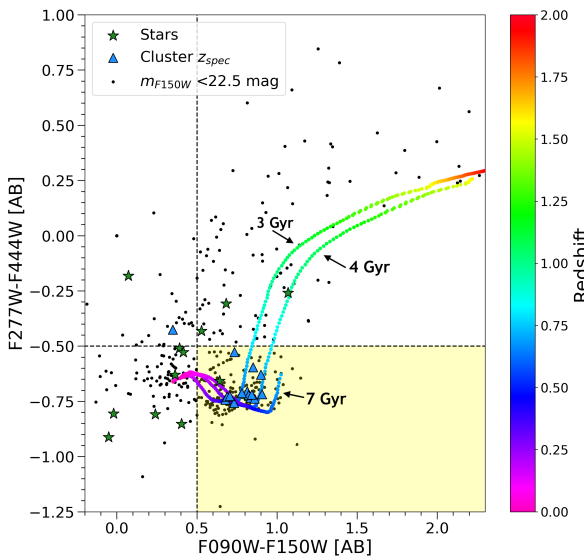


Figure 11. NIRCam color–color plot bracketing the rest-frame $1.6\mu\text{m}$ bump used to select G165 members at $z = 0.35$. Small points show galaxy colors measured by NIRCam. Blue triangles indicate cluster members selected by spectroscopic redshifts, and green stars indicate Milky Way stars. The yellow-filled region in the lower right shows the color-selection area for cluster members. The colored lines shows colors of stellar populations of 3, 4, and 7 Gyr at $0.1 < z < 1.5$ with redshift encoded as shown by the color bar. These colors represent a low-dust elliptical galaxy with no AGN.

5.2. The Arc 1 System: Arcs 1a and NS_46

The spectroscopically-confirmed members of the “Arc 1 system” consist of two galaxies at $z = 2.24$. The spectra of Arc 1a (the DSFG) and Arc NS_46 present many of the emission lines expected of starbursting galaxies. For

each object the ongoing SFR is measured off of the $\text{H}\alpha$ line flux corrected for underlying stellar absorption and for dust extinction by the Balmer decrement method. The values corrected for lensing magnification are $\text{SFR} = 20_{-13}^{+40} \text{ M}_\odot \text{ yr}^{-1}$ and $80_{-37}^{+70} \text{ M}_\odot \text{ yr}^{-1}$ for Arcs 1a and Arc NS_46, respectively, where our lens model estimates $\mu \approx 2.7\text{--}2.9$ for each. The SFRs are both high, and similar to within the uncertainties. Moreover, the two galaxies are closely-separated in radial velocity ($\sim 1400 \text{ km s}^{-1}$), making it tempting to ask if a galaxy interaction may explain the ongoing star formation. An estimate of the dust-obscured SFR, compared to unobscured (e.g. via $\text{H}\alpha$), may be $\sim 50\text{--}90\%$ (Whitaker et al. 2017). From which, we adopt a value of $\sim 75\%$ to represent the obscured, far-IR derived SFR to compare with our $\text{H}\alpha$ -derived SFR. We suspect that the source does not have a 100% dust covering fraction because rest-frame UV light (observed-frame g -band) is detected (Frye et al. 2019). This correction for obscured star formation leads to a rough estimate of the total SFR in Arcs 1a and NS_46 that is still higher by a factor of four.

For Arc 1a, which is the lensed DSFG, a value for the SFR was measured encompassing the different counter-image (Arcs 1b/c), resulting in a total (rest-frame far-infrared luminosity) $\mu\text{SFR} = 12,000\text{--}23,816 \text{ M}_\odot \text{ yr}^{-1}$ (Harrington et al. 2016). The $\text{H}\alpha$ vs far-IR-derived SFR values differ by up to \sim order of magnitude when corrected for the lensing magnification factors obtained by our LTM model of ~ 2.9 and 30 for Arcs 1a and 1b/c, respectively. An attribute that makes their comparison a challenge is that according to the lens model, Arc 1a corresponds to the total integrated starlight of the galaxy whereas Arcs 1b/1c equates only to a small portion of the galaxy light. Thus different regions of the Arc 1 galaxy appear in Arc 1a and Arc 1b/c, respectively. Moreover, the light from Arc 1a is not easily separable from Arc NS_46 (Figure 5). Any cross-contamination of the light would alter the SFR tallies. A detailed lens model that separates out the independent contributions of Arc 1a from Arc NS_46 is beyond the scope of this study, and will be presented in a different paper (Kamienieski et al. 2023, in prep.).

Arcs 1a and NS_46 are classified as star-forming galaxies (SFGs) on account of their high $\text{H}\alpha$ equivalent widths, $\gg 10 \text{ \AA}$ (Li et al. 2023). Balmer family lines are detected in emission all the way up to and including $\text{H}\delta$, and $[\text{O II}]\lambda 3727$ is strongly-detected in emission ($W_{[\text{O III}]} > 5 \text{ \AA}$), thereby further classifying these two sources as short starbursting galaxies (Balogh et al. 1999). On a larger timescale, the $\text{H}\delta$ absorption line

Table 4. Galaxies in Compact Groups at $z \approx 2$

ID	R. A.	Decl.	z_{sp}	m_{F200W}	$E(B - V)$	μ	$\log \mu M^a$	sSFR
	(J2000)	(J2000)		(AB)			(M $_{\odot}$)	(Gyr $^{-1}$)
Arc 2a	11:27:15.34	+42:28:41.05	1.7833 ± 0.0010	20.30	0.22 ± 0.04^c	5.1	11.7	$0.076^{+0.040^d}_{-0.018}$
Arc 2c	11:27:15.98	+42:28:28.72	1.7834 ± 0.0005	20.26	0.20 ± 0.04^c	7.2	11.7	$0.070^{+0.033^d}_{-0.014}$
NS_337	11:27:16.28	+42:28:23.59	1.7810 ± 0.0009	21.77	0.13 ± 0.11^c	2.5	10.7	$_{-e}$
NS_342	11:27:19.46	+42:28:24.79	1.7664 ± 0.0009	24.06	0.01 ± 0.02^c	1.6	9.18	$2.0^{+0.30}_{-0.20}$
Arc 8.2c	11:27:15.89	+42:28:28.90	1.7839 ± 0.0002	26.13	0.24 ± 0.17^b	9.0	8.45	$8.5^{+9.8}_{-3.2}$
NS_123	11:27:04.64	+42:27:15.24	1.7874 ± 0.0003	23.94	0.32 ± 0.05^b	1.5	9.05	$9.6^{+4.3}_{-2.0}$
Arc 9c	11:27:16.11	+42:28:27.99	1.7816 ± 0.0002	26.10	0.31 ± 0.05^b	5.0	7.43	260^{+120}_{-55}
Arc 1a	11:27:13.92	+42:28:35.43	2.2355 ± 0.0003	24.90	0.85 ± 0.25^b	2.9	10.4	$2.3^{+4.5}_{-1.5}$
NS_46	11:27:13.87	+42:28:35.67	2.2401 ± 0.0002	24.04	0.81 ± 0.04^b	2.7	9.51	67^{+57}_{-31}

NOTE—Column 1: lensed source name; Column 2: R. A.; Column 3: Decl.; Column 4: NIRSpec spectroscopic redshift; Column 5: F200W apparent magnitude; Column 6: Color excess due to reddening; Column 7: lensing magnification factor estimated from our lens model; Column 8: stellar mass as estimated from the FAST++ model, which is uncorrected for lensing magnification μ ; Column 9: specific star formation rate.

^a Masses are assigned a minimum uncertainty of 0.1 dex to account for systematics (Leja et al. 2019a,b).

^b Measured directly from Balmer decrement

^c Derived from FAST++ SED fit

^d Corrected for incomplete slit coverage of the source.

^e Measurement of H α line flux is not possible for this object.

that typically appears in galaxies with star formation within the past 800 Myr is undetected in this data set (Goto 2007; Weibel et al. 2023).

Taken together with its star-bursting galaxy classification, high $E(B - V)$ value that is close to unity, and high metal enrichment levels, this galaxy pair overall shows some physical properties expected of a DSFG. For each galaxy in the pair the bulk of the star formation is recent ($\lesssim 5$ Myr), and possibly triggered by the interaction of Arc 1a with Arc NS_46. If this is the case then a galaxy-galaxy interaction may have also instigated any AGN activity. The measured and estimated internal properties of Arcs 1a and NS_46 are reported in Table 4.

5.3. The Arc 2 system: Arc 2, NS_337, NS_342, NS_123, 8.2c, and 9c

The “Arc 2 system” consists of Arc 2 (the SN host) and five other galaxies all at $z = 1.78$. Particular to Arcs 2a and 2c, nearly two dozen emission and absorption line features are identified (Figure 4). Notably, for each image H α is in emission while H β is in absorption, making the Balmer decrement method of estimating dust extinction unavailable. Thus for these two galaxy images the H α line flux was corrected for both underlying stellar absorption and for dust extinction from the

FAST++ fit. The H α line flux was further corrected for incomplete slit coverage of the source as described in §5.1. For Arcs 2a and 2c, we measured correction factors of 1.2 ± 0.05 and 3.9 ± 0.26 , respectively. The SFR was then computed and then divided by the stellar mass. The stellar mass is $(5.0 \pm 0.1) \times 10^{11} \text{ M}_{\odot}$ for both galaxy images, the highest of any other galaxy in this group at this redshift, while the sSFR has the lowest value of its cohort.

The most conspicuous difference between the two galaxy images of this same lensed source is the high apparent brightness of Arc 2a (Figure 4). This is the case despite the fact that Arc 2c has a higher magnification factor. As can be seen in the MSA footprint (Figure 4, right-hand column) different regions of the galaxy are sampled in Arcs 2a and 2c, and in neither one does the slit cover the entire lensed source. In particular, the MSA slit for Arc 2a covers more of the central nuclear region of the arc, which may explain its higher brightness. Some clues may also be drawn from the rather different values for D(4000) of 1.91 ± 0.05 and 1.54 ± 0.03 for Arcs 2a and Arc 2c, respectively. It is interesting to ask if this 30 % difference may be a consequence of the MSA slit sampling a brighter central region that contains a higher fraction of stars in the emerging bulge galaxy component.

On galaxy classification, the $\text{H}\alpha$ emission line indicates that at least some of the star formation is ongoing, and we measure $W_{[\text{OII}]} > 5 \text{ \AA}$ that corroborates this star-forming galaxy classification (Balogh et al. 1999). However, although $\text{H}\delta$ is detected in absorption, a feature that is typically associated with galaxies which have undergone star formation within the past 800 Myr, it is weak ($W_{\text{H}\delta} < 5 \text{ \AA}$), possibly indicating that A- and early F-type stars are not yet dominating the spectrum (Goto 2007; Weibel et al. 2023). There is a strong NaD line, which in combination with the higher D(4000) values indicate the presence of an older stellar population that formed within $\sim 2 \text{ Gyr}$ (Wang & Lilly 2020). We note that the possibility of a post starburst (PSB) galaxy sub-category is generally ruled out by presence of $\text{H}\alpha$ and $[\text{O II}]\lambda 3727$ in emission (Li et al. 2023, and references therein).

The NaD absorption line is stronger in Arc 2 than for any other members in its $z = 1.78$ group, and may consist of both a stellar and an outflowing gas component (Cazzoli et al. 2016). Another prominent feature that is relatively rare at $z \sim 2$ is the detection of all three lines of CaT that is associated with cool stellar atmospheres (Cenarro 2003). Of the culprits, supergiants would dominate the flux density budget, and may be another indicator of a previous star forming episode in this galaxy's more distant past ($\gtrsim 1 \text{ Gyr}$). In sum, Arcs 2a and 2c are best-fit to a moderately dusty and massive star-forming galaxy that appears to have already assembled much of its stellar mass by $z = 1.78$, a result that also matches the findings in Polletta et al. (2022).

Arc NS_337 is apparently IR-bright ($m_{F200W} = 21.77 \text{ AB mag}$). The prominent spectral features are detected in absorption except for He I, which is a common feature detected in nearly all of the $z = 2$ spectra in our sample. The computation of the SFR based on the $\text{H}\alpha$ emission line is not available for this source. By its low $W_{\text{H}\delta} < 5 \text{ \AA}$ and $W_{[\text{OII}]} < 5 \text{ \AA}$, this galaxy is classified as passive, although the value of D(4000)= 1.39 ± 0.019 places it near the border with an SFG (Balogh et al. 1999). The addition of the low $W_{\text{H}\alpha} < -3 \text{ \AA}$ along with the low $W_{[\text{OII}]}$ and $W_{\text{H}\delta}$ also disqualifies it as a PSB galaxy (Li et al. 2023, and references therein).

Regarding its age, the $\text{H}\alpha$ emission line is absent, implying at best only minimal ongoing star formation. Similar to Arc 2, $\text{H}\delta$ is detected in absorption, but is weak ($W_{\text{H}\delta} < 5 \text{ \AA}$), indicating that some star formation took place in the past $\sim 800 \text{ Myr}$. There is a strong NaD line and a moderately-strong 4000 \AA continuum break D(4000) value, which indicate the presence of an older stellar population that formed within $\sim 2 \text{ Gyr}$ (Wang & Lilly 2020). Interestingly, similar to Arc 2 CaT is de-

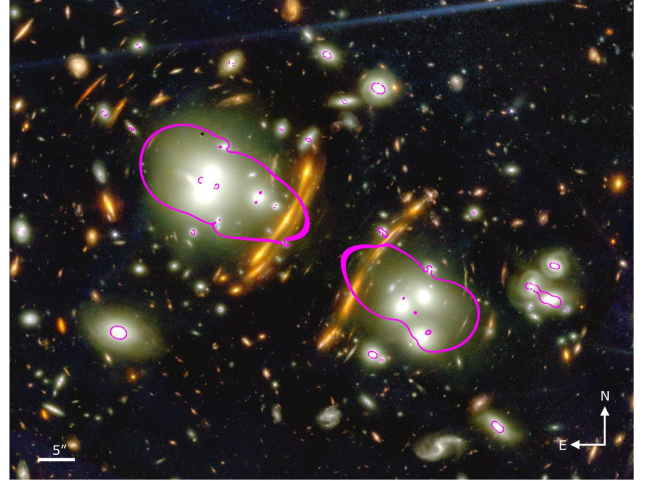


Figure 12. Color image using all NIRCam filters showing the central region of the G165 cluster. Magenta curves depict the $z = 2$ tangential critical curve obtained from our LTM model, and white labels show the image scale and orientation. Several giant arcs merge with the critical curve, an attribute that may assist with the detection of transients. The lens model separates out the NE and SW cluster cores at this redshift. The color rendering is the same as Figure 3.

tected, possibly uncovering an underlying population of giants/supergiants left over from an older epoch of star formation. The FAST++ fits estimate low dust extinction that is 1 dex lower than Arc 2, and a stellar mass that is an order of magnitude lower than Arc 2. Overall, Arc NS_337 is a second relatively massive galaxy in this $z = 1.78$ group, and by a spectroscopic analysis appears to be quiescent.

Arcs NS_342, NS_123, Arc 8c, and Arc 9c are emission-line galaxies with higher stellar activity levels, making them more akin to the $z = 2.24$ group spectra discussed in §5.2. $\text{H}\alpha$ and $\text{H}\beta$ are detected in emission for most cases, enabling measurement of the SFR based off of the $\text{H}\alpha$ line fluxes corrected for underlying stellar absorption from a FAST++ fit, and for dust extinction by the Balmer decrement method. For Arc NS_342 where $\text{H}\beta$ is not detected in emission, we extract the value for A_V from our FAST++ model fit. Relative to Arc 2, the sSFRs are all at least an order of magnitude higher, and the stellar masses are all \sim two orders of magnitude lower.

These four galaxies are all classified as SFGs based on the negative D(4000) values, and the high values of $W_{[\text{OII}]} > 5 \text{ \AA}$ and $W_{\text{H}\alpha} > 10 \text{ \AA}$ (Balogh et al. 1999; Li et al. 2023). For Arc 9c the Balmer family lines are detected in emission all the way through $\text{H}\delta$. For Arcs 8.2c and 9c we measure ($W_{\text{H}\delta} < 0 \text{ \AA}$) as well as ($W_{[\text{OII}]} > 5 \text{ \AA}$), further classifying these two sources as short starbursting galaxies (Balogh et al. 1999). To get

their classifications by the optical diagrams, the flux ratios R_3 , N_2 , S_2 and $[\text{O I}]\lambda 6300/\text{H}\alpha$ place Arc NS_342 and Arc 9c in the star forming (SF) region, Arc 8.2c in the SF/composite region, and Arc NS_123 in the AGN (subclass Seyfert) region (Mingozi et al. 2023). We note that only NS_123 shows evidence of having a predominantly harder source of ionizing flux normally associated with AGNs.

The presence of several rest-frame optical emission lines enables estimates of the gas-phase oxygen abundance. Ratios of emission line fluxes are computed for several of the line ratios and combinations of line ratios defined in §5.2 with the exception of Arc NS_342, whose diagnostic line ratios only include N_2 and S_2 since $\text{H}\beta$ is found to be in absorption even after accounting for underlying stellar absorption and correction dust extinction. We obtain values for these four galaxies in the range of $12 + \log(\text{O/H}) = 8.3\text{--}8.6$. These sources have on average stellar masses and metallicities which place them higher than the mean relation correlating in Sloan Digital Sky Survey (SDSS) galaxies, the so-called “mean metallicity” relation (i.e., Curti et al. 2020). Taken together with their high SFRs, it is interesting to ask if these counterparts of Arc 2 are intercepted during an epoch of a relatively-rapid build-up of stellar material. We refer to §6.2 for further discussion on the evolutionary state of this compact galaxy group.

6. DISCUSSION

6.1. G165 Cluster Properties

In a 1-D trace of the surface-mass density (Figure 13), the two peaks correspond to the cluster cores, and each core further separates out into more minor peaks that trace individual cluster members. An overall depression appears between the two peaks in the 1-D trace, but not a sharp cutoff. We measure an angular separation between the cluster cores of $38''$ equating to 200 kpc at the redshift of the cluster. Inside of each core are two radio galaxies, with the two examples in the NE component further distinguished by showing extended head-tail morphologies consisting of tails aligned \sim parallel to each other (Pascale et al. 2022, and references therein). Assuming a radial velocity of 600 km s $^{-1}$ typical of head-tail galaxies (Venkatesan et al. 1994), and that the radial velocity is similar in magnitude to the transverse velocity component, these quantities yield a crossing time of \sim 300 Myr. We note that the mean velocity difference of the two cluster core components is not well constrained given the current data set (Pascale et al. 2022). Redshifts of additional cluster members are needed to measure and/or better constrain the cluster velocity configuration.

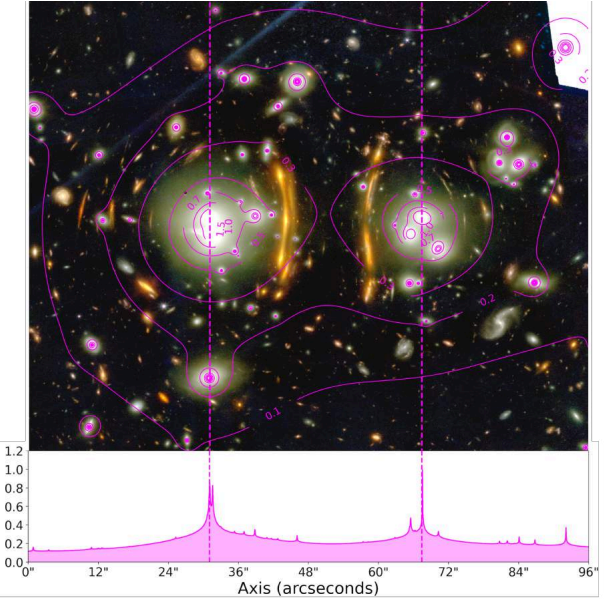


Figure 13. G165 mass distribution from our lens model. Pink contours in the upper panel show the surface-mass (κ) contours scaled to the critical value. The image is oriented as Figure 2. The lower panel depicts the 1-D mass distribution summed over $78''$ ($=390$ kpc) orthogonal to the collision axis. The value for κ is summed up over the full field of view depicted in the diagram, which covers an angular range of $96''$ ($=480$ kpc). The NE and SW component mass peaks are marked with long-dashed vertical lines, and there is a modest depression between them.

Pascale et al. (2022) report a relatively large offset in the centroid position of the luminosity of the spectroscopically-confirmed cluster members which points to a major disturbance of the cluster. The velocity offset of the BCG from the systemic redshift of the cluster is another diagnostic of cluster virialization (Rumbaugh et al. 2018). The BCG’s measured redshift of 0.3376 was originally drawn from the SDSS DR 17 archives and is independently-confirmed by the MMT/Binospec spectroscopy presented in this paper (Table 3). We herein confirm that both the brightest and the largest galaxy in the cluster entire (considering both the NE and SW components) is significantly-blueshifted from the cluster’s systemic velocity (\sim 3400 km s $^{-1}$) that would place it near the outskirts of the cluster.

One possible scenario is that the BCG is falling in towards the cluster from behind, such that the blueshift of the BCG and the redshift of the cluster are both \sim 1700 km s $^{-1}$ relative to the velocity mean between the two of them. This relative newcomer to the cluster would not be detectable by our lens model as a subhalo within the NE component because the lens redshift is so similar. Moreover, the BCG is one of the two head-

tail radio sources, from which we infer that interactions with the intercluster medium are already imprinting the extended tails in the wake of its motion. This head-tail radio emission is less extended than the other cluster galaxy immediately to the north (see Pascale et al. (2022), their Figure 14). This possibly supports the view that the BCG is primarily falling along the line of sight towards the cluster rather than transversely, although it could also have a less-active nucleus. We note that for another merging cluster, El Gordo, the BCG was also significantly offset from the cluster's systematic velocity ($\sim 2400 \text{ km s}^{-1}$) (Frye et al. 2023). XMM/Newton observations are approved for G165 (AO22, PID #92030, PI: Frye), which promise to offer some insights regarding its overall dynamical state by mapping out the mass distribution and searching for shocks.

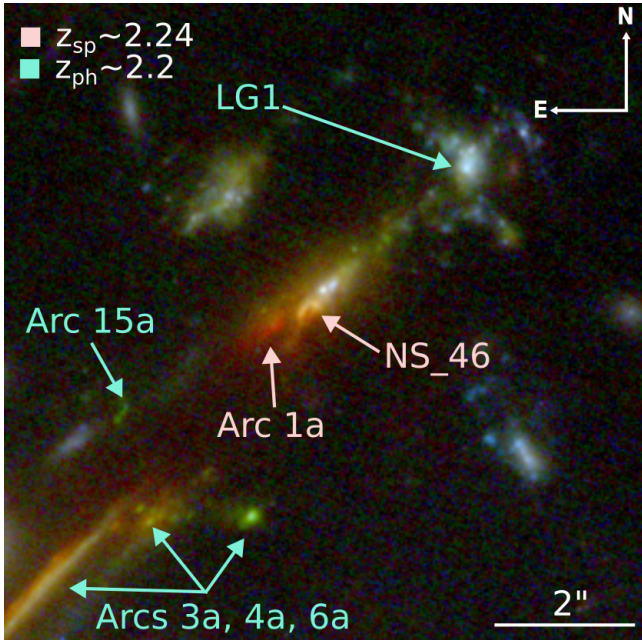


Figure 14. The Arc 1a galaxy group at $z \sim 2.2$. Photometric redshift fits identify a compact galaxy overdensity at $z \sim 2.2$ that surrounds the spectroscopically confirmed Arcs 1a and NS_46 consisting of a total of 6 objects. These include the multiply imaged Arcs 3, 4, 6, and 15, as well a singly imaged lensed galaxy located only 20 kpc away from Arc 1a and NS_46. Each galaxy exhibits a highly clumpy morphology consistent with cosmic-noon starbursts, and if their redshifts are correct, they may be interacting given their ~ 20 kpc physical separations (after demagnification according to our lens model).

6.2. Compact Galaxy Groups & Associations

Three peaks in the background galaxy distribution merit special attention (Figure 10). They correspond to: (1) a galaxy association centered in projection on

the lensed DSFG Arc 1a at $z_{\text{sp}} = 2.24$ (Figure 14), (2) a galaxy group centered at $z_{\text{sp}} = 1.78$ on the SN host Arc 2 (Figure 3), and (3) a galaxy association centered at $z_{\text{ph}} = 1.65$ located in the PEARLS G165 parallel field (Figure 15). These groups each have a different set of physical properties, as we discuss below.

The Arc 1 Group: NIRSpec spectroscopy uncovers not just the DSFG (Arc 1a) but also a second galaxy proximate to Arc 1a at a velocity separation of 1400 km s^{-1} that appears to be the second member of an interacting galaxy pair (see Figure 5 and § 6.2). Such interactions are expected to be common at cosmic noon (e.g., Conselice 2006), and may explain the star formation rates, corrected for lensing magnification of $\gtrsim 20 \text{ M}_\odot \text{ yr}^{-1}$ for each one (Table 4). This galaxy pair is flanked by 5 other galaxies photometrically constrained to a similar redshift of $z \sim 2.2$ (Figure 14). They include triply-imaged Arc systems 3, 4, 6, and 15, and a single galaxy image that we call LG1. These other galaxies have clumpy morphologies and blue colors consistent with active star-formation. Our lens model predicts for Arcs 1a, 3a, 4a, and 15a to be contained within a physical extent in the source plane of 20 kpc, and all of them to be contained within 40 kpc.

If this tight configuration of galaxies is real, then combined with the evidence of starbursting activities in its two central members, it is possible that all seven of these galaxies may be engaged in interactions. The galaxies are expected to grow by star formation perhaps supplied by cold gas streams from the IGM (Dekel et al. 2009) and/or by galaxy mergers (Ellison et al. 2008; Scudder et al. 2012; Ellison et al. 2022). It is interesting to ask if we may be witnessing the “preprocessing” of the galaxy members, by which we mean that their stellar masses are built up prior to virialization and quenching (Rennahan et al. 2020; Sengupta et al. 2022). The answer to this question requires spectroscopy of the participating members to extract their physical and star-forming properties, and so cannot be fully addressed with this data set. IFU spectroscopy in rest-frame UV and rest-frame optical would yield star formation rates and/or Lyman- α detections for all seven members that would confirm group membership and provide further insights into its evolutionary state.

The Arc 2 Group: By far the dominant peak in the background galaxy redshift distribution is at $z = 1.78$ (Fig 10). Hundreds of photometrically-selected galaxies with this redshift are distributed across the field of view of our NIRCam observations of $\sim 1.5 \times 2.5 \text{ Mpc}$ at $z = 1.78$ (Figure 10). This redshift is so common that it extends to about one-quarter of the image systems as well: Arcs 2, 8, 9, 10, and 16 (Table A1). If real, then

this galaxy overdense region effectively provides a grid of bright background $z \sim 2$ sources which may explain the abundance of giant arcs and image multiplicities in the field of this otherwise lower-mass example of a galaxy cluster.

Of the six spectroscopically-confirmed galaxies at this redshift, our lens model estimates that the innermost four galaxies Arcs 2, 8, 9, and NS_337 labeled in Figure 3 have a physical extent in the source plane of $\lesssim 33$ kpc, with the SN host Arc 2 at the group center. These same four galaxies have a velocity spread of 900 km s^{-1} . The small spatial and radial velocity extents confirm the presence of a compact galaxy group at $z = 1.78$ (Table 4).

All but Arc 2 and Arc NS_337 have high sSFRs $\gtrsim 1 \text{ Gyr}^{-1}$. Arc 2 not only has a relatively low rate of ongoing star formation, but also shows little evidence of star formation in the past $\sim 1 \text{ Gyr}$ (§5.3). Moreover, Arc 2 has a stellar mass that is 1–2 orders of magnitude higher than the other spectroscopically-confirmed members. It is interesting to ask if Arc 2 has already settled down after having built up the majority of its stellar mass, and is now surrounded by star-forming satellite dwarfs, potentially consistent with the picture of “downsizing” in hierarchical galaxy formation (Neistein et al. 2006; Fontanot et al. 2009; Oser et al. 2010).

The $z = 1.65$ parallel field: The third group of galaxies is located at $z \sim 1.65$, and was uncovered in a photometric redshift search in the parallel field (Figure 15). These galaxies exhibit similar red colors, and on visual inspection all but one have apparent elliptical morphologies. The morphology hints that the red color is a result of older stellar populations rather than dust, a scenario that is supported by our best-fit SED models. If so, then this galaxy association may consist mainly of quiescent galaxies.

These galaxies have relatively high masses of $10^{10-11} M_{\odot}$ as estimated off of the SED models, stellar ages of $\gtrsim 1 \text{ Gyr}$, and little to no dust extinction with the exception of the one SFG (yellow arrow in Figure 15). This is consistent with the scenario of a build-up of stellar material at higher redshifts ($z \gtrsim 3$), followed by gas exhaustion at $z \lesssim 1.5$ just prior to an epoch characterized more by hierarchical growth (i.e., Rennehan et al. 2020). Spectroscopy is needed to confirm that this photometrically-identified galaxy association is a bona fide galaxy group, and may also yield better estimates of the SFR and dust extinction to corroborate this high-redshift quiescent galaxy group picture.

Supernova Rate at $z = 2$: The total instantaneous ($\text{H}\alpha$ -based) SFR in our NIRSpec sample that is corrected for lensing magnification (and dust obscuration

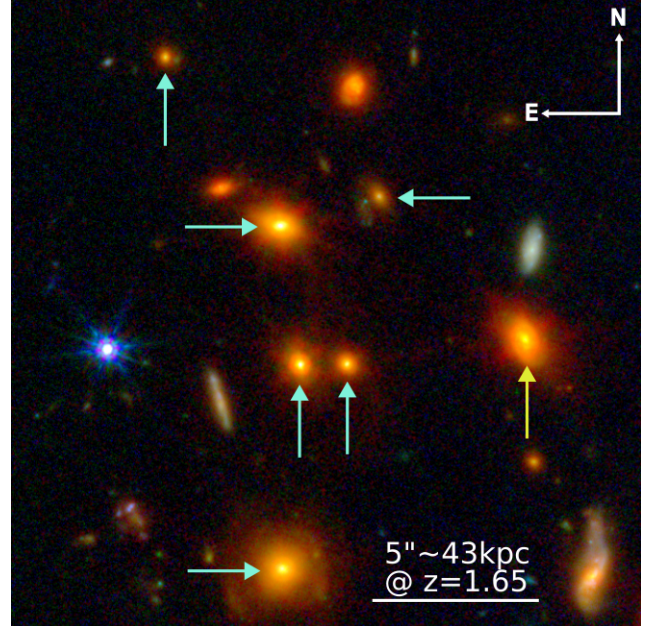


Figure 15. The $z = 1.65$ galaxy group. Photometric redshifts identified a group of seven galaxies within $15'' \pm 20''$ in the G165 NIRCam parallel field. These galaxies broadly share similar colors and morphology, and photometric SED fitting finds all but one (yellow arrow) to be quiescent. These galaxies have a total physical extent of $\lesssim 130$ kpc, making them another potential compact galaxy group.

for Arcs 1a and NS_46) and integrated over both the Arc 1 and Arc 2 galaxy groups is $\gtrsim 500 M_{\odot} \text{ yr}^{-1}$. Although a rough correction has already been made to account for dust obscuration (§5.2) it is likely to be conservative, especially for the starbursting galaxies Arc 1a and Arc NS_46, which are especially dusty. In addition, there are other lensed galaxies at the same (photometric) redshift that could be star-forming but require spectroscopic confirmation, such as Arcs 3, 4, 6, and 15. All of the above makes this SFR likely to be an underestimate of the true value. The SFR derived from the far-infrared luminosity Harrington et al. (2016) (corrected for magnification) of $400-800 M_{\odot} \text{ yr}^{-1}$ uses spatially unresolved *Herschel* photometry covering Arc 1a and Arc 1b/c (including Arcs 3, 4, 6, 15). At the same time only a portion of Arc 1a is imaged into Arc 1b/c. It should be emphasized that a direct one-to-one comparison between these two SFRs derived by two different methods and applied to two different arcs is not entirely fair without near-IR spectroscopy of Arc 1b/c to serve as a calibration.

Following the prescription in Young et al. (2008), and bracketing the two results ($\text{H}\alpha$ and FIR-derived SFRs), we estimate a lower limit on the rate of core-collapse (CC) SNe $\gtrsim 1-2 \text{ SNe yr}^{-1}$. This value is consistent with results in ? in which CC SNe are summed up over the six

Hubble Frontier Fields (Lotz et al. 2017). They found that with an JWST/NIRCam imaging cadence four 1-hour visits per year, the summed total rate integrated over all six HFFs is expected to be ~ 0.9 CC SNe and 0.06 SNe Ia in F150W. Thus making regular monitoring of the G165 cluster alone may potentially be well-rewarded with the discovery of additional SNe.

7. CONCLUSIONS AND FUTURE DIRECTIONS

This overview study presented the full set of JWST observations in the field of G165. A transient was identified in the PEARLS Epoch 1 NIRCam imaging relative to previous HST imaging (Figure 7). This point-source was situated 1.5-2kpc in the source plane from the massive infrared-bright galaxy Arc 2 at $z = 1.78$ that is taken to be the SN host. Three different images of the Arc 2 plus SN pair were detected in the NIRCam imaging, and the pair flipped in parity with each crossing of the critical curve, as predicted by lensing theory. The three points had a fit to the light curve expected of a SN Type Ia (Figure 8).

We identified 21 image systems which are used to construct the first NIRCam-based LTM lens model, which amounts to nearly a factor of two increase in the number of image system constraints over previous works. Model inputs included 161 cluster members which were carefully selected by spectroscopy (where available), and the $1.6\ \mu\text{m}$ bump. On completing the first NIRCam-based lens model, we confirm the bimodal mass distribution. We also measure a mass within 600 kpc of $(2.6 \pm 0.30) \times 10^{14}\ M_{\odot}$ that is consistent with previous results also obtained by the LTM approach.

NIRSpec spectroscopic redshifts were measured for 30 lensed sources, which included all three appearances of the SN, two of the three images of Arc 2, image systems 1, 5, 8, and 9, and other lensed sources. A spectrum of the BCG was also obtained using MMT/Binospec that confirmed it to be offset from the cluster systemic velocity by $\sim 3400\ \text{km s}^{-1}$, which we take to be evidence of a major cluster disturbance. The spectroscopic redshifts are presented in this paper (Tables 2 and 3). The focus of the spectroscopic analysis was on the galaxies at the same redshift as Arc 1 ($z = 2.24$) and Arc 2 ($z = 1.78$). These two systems of galaxies appear to be representatives of larger galaxy overdensities at these same redshifts, an assertion that is backed up by minor peaks in the photometric redshift distributions.

On the Arc 1 system, in a spectroscopic analysis and FAST++ fit to Arc 1a and its counterpart Arc NS_46, we measure relatively-high dust levels and high *ongoing* sSFRs expected of starbursting galaxies. By computing the relevant line ratios across the rest-frame optical

spectrum we find some evidence for AGN activity, and near-solar gas-phase oxygen abundances. Meanwhile, by other diagnostic absorption line features we infer the lack of significant star formation integrated over longer time scales, $\lesssim 1$ Gyr. Our photometric redshift estimates pick out an additional five lensed sources characterized by clumpy star formation and situated within a spatial extent of 40 kpc in a group that includes Arcs 1a and NS_46. If real, then we speculate that this compact set of seven galaxies may be intercepted during an epoch of active star formation, a hypothesis that can be tested by obtaining additional and ideally IFU-based spectroscopy to characterize the star-formation in the various clumps/knots contained in each galaxy.

Regarding the Arc 2 system, in a spectroscopic analysis and a FAST++ fit to Arcs 2a, 2c and to its galaxy neighbors confirmed by NIRSpec which are Arcs NS_337, NS_342, 8.2c, 9c, and NS_123 (Figure 4), a stark contrast was unveiled between SN host Arc 2 and the other group members. Arc 2 dominates the stellar mass $((5.01 \pm 0.10) \times 10^{11}\ M_{\odot})$, has a much lower sSFR ($\text{sSFR}_{\text{Arc2a}} = 0.076^{+0.040}_{-0.018}\ \text{Gyr}^{-1}$), and has only small amounts of ongoing star formation, which peters off to still lower amounts integrated out to ~ 1 Gyr. At the same time, Arcs 8.2c, 9c and NS_123 are emission-line sources which are on average 1–2 orders of magnitude less massive, yet have ~ 2 orders of magnitude higher values of ongoing SFRs scaled to their masses. Arcs 2, NS_337, 8.2c and 9c are separated in velocity $\sim 900\ \text{km s}^{-1}$ and are situated within a spatial extent of 33 kpc. We infer that Arc 2 may be an example of a massive galaxy that has completed a star formation episode ~ 1 Gyr ago and that is now surrounded by star-forming satellite dwarfs, consistent with a galaxy downsizing scenario.

The next steps focus on SN H0pe. The NIRSpec spectroscopy of SN H0pe will be presented in an upcoming paper that confirms its classification as a Type Ia SN and measures a value for the spectroscopic time delay (Chen et al. 2023, in prep.). The full NIRCam photometry of the SN measured across all three observing epochs (and hence all 9 points on the light curve) that accounts for the subtraction of the Arc 2 galaxy halo light and correction for any microlensing effects, and a measurement of the photometric value for the time delay will appear in a different paper (Pierel et al. 2023, in prep.). Meanwhile, a more detailed lens model that performs a full surface brightness reconstruction of Arc 2 will take the next step in improving on the SN photometry (Caminha et al. 2023, in prep.). These efforts are complemented by a focused study on the dust extinction of Arc 2, which impacts understanding of the SN physics (Johansson et

al. 2023, prep.). A separate lens modeling investigation will focus on the compact galaxy group surrounding the DSFG Arc 1 (Kamieneski et al. 2023, in prep.), and another will focus on a more detailed spectroscopic analysis of the line features (Foo et al. 2023, in prep.). A project is also underway to carry out a spectroscopic analysis of the quiescent lensed galaxy Arc NS274 (Valentino et al. 2023, in prep.). And finally, the time delay estimates generated from the lens models, the photometry, the spectroscopy, and the weighted combination of all time delay estimates from these models will be used to measure a value for H_0 (Pascale et al. 2023, in prep.). Given the high rate of ongoing star formation across this cluster of $\gtrsim 400 \text{ M}_\odot \text{ yr}^{-1}$, regular monitoring of the G165 field may be well-rewarded with the discovery of new SNe and other transients.

This paper is dedicated to PEARLS team member and collaborator Mario Nonino, whose enthusiasm for the science and generosity have been an inspiration for us. B.L.F. was funded by NASA JWST DD grant (PID 4446; PI: Frye) from the Space Telescope Science Institute (STScI). B.L.F. obtained student support through a Faculty Challenge Grant for Increasing Access to Undergraduate Research, and the Arthur L. and Lee G. Herbst Endowment for Innovation and the Science Dean’s Innovation and Education Fund, both obtained at the University of Arizona. R.A.W. was funded by NASA JWST Interdisciplinary Scientist grants NAG5-12460, NNX14AN10G, and 80GNSSC18K0200 from NASA Goddard Space Flight Center. We thank the JWST Project at NASA GSFC and JWST Program at NASA HQ for their many-decades long dedication to make the JWST mission a success. We especially thank Peter Zeidler, Patricia Royale, Tony Roman, and the JWST scheduling group at STScI for their continued dedicated support to get the JWST observations scheduled. This work is based on observations made with the NASA/ESA/CSA James Webb Space Telescope. The data were obtained from the Mikulski Archive for Space Telescopes (MAST) at the STScI, which is operated by the Association of Universities for Research in Astronomy, Inc., under NASA contract NAS 5-03127 for JWST. These observations are associated with JWST programs 1176 and 4446. This work is also based on observations made with the NASA/ESA *Hubble Space Telescope* (HST). The data were obtained from the Barbara A. Mikulski Archive for Space Telescopes (MAST) at the STScI, which is operated by the Association of Universities for Research in Astronomy (AURA) Inc., under NASA contract NAS 5-26555 for HST.

Software: SourceExtractor: (Bertin & Arnouts 1996) <https://www.astromatic.net/software/sextarator/> or <https://sextractor.readthedocs.io/en/latest/>

Software: JWST calibration pipeline version 1.11.2 (Bushouse et al. 2022) <https://zenodo.org/badge/DOI/10.5281/zenodo.8140011.svg>

Software: FAST++ Kriek et al. (2009) <https://github.com/cschreib/fastpp>

Software: SPECUTILS Earl et al. (2023)

Facilities: Hubble Space Telescope, James Webb Space Telescope, Mikulski Archive <https://archive.stsci.edu>, MMT/Binospec, MMT/Hectospec, VLA, LOFAR

REFERENCES

Adams, N. J., Conselice, C. J., Ferreira, L., et al. 2023, MNRAS, 518, 4755, doi: [10.1093/mnras/stac3347](https://doi.org/10.1093/mnras/stac3347)

Arnouts, S., & Ilbert, O. 2011, LePHARE: Photometric Analysis for Redshift Estimate, Astrophysics Source Code Library, record ascl:1108.009. <http://ascl.net/1108.009>

Bagley, M. B., Finkelstein, S. L., Koekemoer, A. M., et al. 2022, arXiv e-prints, arXiv:2211.02495. <https://arxiv.org/abs/2211.02495>

Baldwin, J. A., Phillips, M. M., & Terlevich, R. 1981, PASP, 93, 5, doi: [10.1086/130766](https://doi.org/10.1086/130766)

Balogh, M. L., Morris, S. L., Yee, H. K. C., Carlberg, R. G., & Ellingson, E. 1999, ApJ, 527, 54, doi: [10.1086/308056](https://doi.org/10.1086/308056)

Bertin, E., & Arnouts, S. 1996, A&AS, 117, 393, doi: [10.1051/aas:1996164](https://doi.org/10.1051/aas:1996164)

Brammer, G. 2021, eazy-py, 0.5.2, doi: [10.5281/zenodo.5012704](https://doi.org/10.5281/zenodo.5012704)

Brammer, G. B., van Dokkum, P. G., & Coppi, P. 2008, ApJ, 686, 1503, doi: [10.1086/591786](https://doi.org/10.1086/591786)

Broadhurst, T., Benítez, N., Coe, D., et al. 2005, ApJ, 621, 53, doi: [10.1086/426494](https://doi.org/10.1086/426494)

Bushouse, H., Eisenhamer, J., Dencheva, N., et al. 2022, JWST Calibration Pipeline, 1.11.2, Zenodo, doi: [10.5281/zenodo.8140011](https://doi.org/10.5281/zenodo.8140011)

Cañameras, R., Nesvadba, N. P. H., Guery, D., et al. 2015, A&A, 581, A105, doi: [10.1051/0004-6361/201425128](https://doi.org/10.1051/0004-6361/201425128)

Cañameras, R., Nesvadba, N. P. H., Limousin, M., et al. 2018, A&A, 620, A60, doi: [10.1051/0004-6361/201833679](https://doi.org/10.1051/0004-6361/201833679)

Calzetti, D., Armus, L., Bohlin, R. C., et al. 2000, ApJ, 533, 682, doi: [10.1086/308692](https://doi.org/10.1086/308692)

Casey, C. M., Scoville, N. Z., Sanders, D. B., et al. 2014, ApJ, 796, 95, doi: [10.1088/0004-637X/796/2/95](https://doi.org/10.1088/0004-637X/796/2/95)

Casey, C. M., Cooray, A., Killi, M., et al. 2017, ApJ, 840, 101, doi: [10.3847/1538-4357/aa6cb1](https://doi.org/10.3847/1538-4357/aa6cb1)

Cazzoli, S., Arribas, S., Maiolino, R., & Colina, L. 2016, A&A, 590, A125, doi: [10.1051/0004-6361/201526788](https://doi.org/10.1051/0004-6361/201526788)

Cenarro, A.-J. 2003, PASP, 115, 504, doi: [10.1086/374201](https://doi.org/10.1086/374201)

Coe, D., Umetsu, K., Zitrin, A., et al. 2012, ApJ, 757, 22, doi: [10.1088/0004-637X/757/1/22](https://doi.org/10.1088/0004-637X/757/1/22)

Conselice, C. J. 2006, ApJ, 638, 686, doi: [10.1086/499067](https://doi.org/10.1086/499067)

Curti, M., Mannucci, F., Cresci, G., & Maiolino, R. 2020, MNRAS, 491, 944, doi: [10.1093/mnras/stz2910](https://doi.org/10.1093/mnras/stz2910)

Curti, M., Maiolino, R., Carniani, S., et al. 2023, arXiv e-prints, arXiv:2304.08516, doi: [10.48550/arXiv.2304.08516](https://doi.org/10.48550/arXiv.2304.08516)

Dekel, A., Sari, R., & Ceverino, D. 2009, ApJ, 703, 785, doi: [10.1088/0004-637X/703/1/785](https://doi.org/10.1088/0004-637X/703/1/785)

Domínguez, A., Siana, B., Henry, A. L., et al. 2013, ApJ, 763, 145, doi: [10.1088/0004-637X/763/2/145](https://doi.org/10.1088/0004-637X/763/2/145)

Earl, N., Tollerud, E., O'Steen, R., et al. 2023, astropy/specutils: v1.11.0, v1.11.0, Zenodo, doi: [10.5281/zenodo.8049033](https://doi.org/10.5281/zenodo.8049033)

Ellison, S. L., Patton, D. R., Simard, L., & McConnachie, A. W. 2008, AJ, 135, 1877, doi: [10.1088/0004-6256/135/5/1877](https://doi.org/10.1088/0004-6256/135/5/1877)

Ellison, S. L., Wilkinson, S., Woo, J., et al. 2022, MNRAS, 517, L92, doi: [10.1093/mnrasl/slac109](https://doi.org/10.1093/mnrasl/slac109)

Fontanot, F., De Lucia, G., Monaco, P., Somerville, R. S., & Santini, P. 2009, MNRAS, 397, 1776, doi: [10.1111/j.1365-2966.2009.15058.x](https://doi.org/10.1111/j.1365-2966.2009.15058.x)

Frye, B., Pascale, M., Qin, Y., et al. 2019, The Astrophysical Journal, 871, 51, doi: [10.3847/1538-4357/aaeff7](https://doi.org/10.3847/1538-4357/aaeff7)

Frye, B. L., Pascale, M., Foo, N., et al. 2023, ApJ, 952, 81, doi: [10.3847/1538-4357/acd929](https://doi.org/10.3847/1538-4357/acd929)

Galametz, A., Grazian, A., Fontana, A., et al. 2013, ApJS, 206, 10, doi: [10.1088/0067-0049/206/2/10](https://doi.org/10.1088/0067-0049/206/2/10)

Gladders, M. D., & Yee, H. K. C. 2000, AJ, 120, 2148, doi: [10.1086/301557](https://doi.org/10.1086/301557)

Goto, T. 2007, MNRAS, 381, 187, doi: [10.1111/j.1365-2966.2007.12227.x](https://doi.org/10.1111/j.1365-2966.2007.12227.x)

Harrington, K. C., Yun, M. S., Cybulska, R., et al. 2016, MNRAS, 458, 4383, doi: [10.1093/mnras/stw614](https://doi.org/10.1093/mnras/stw614)

Horne, K. 1986, PASP, 98, 609, doi: [10.1086/131801](https://doi.org/10.1086/131801)

Hsiao, E. Y., Conley, A., Howell, D. A., et al. 2007, ApJ, 663, 1187, doi: [10.1086/518232](https://doi.org/10.1086/518232)

Johnson, T. L., & Sharon, K. 2016, ApJ, 832, 82, doi: [10.3847/0004-637X/832/1/82](https://doi.org/10.3847/0004-637X/832/1/82)

Kelly, P. L., Rodney, S., Treu, T., et al. 2023a, Science, 380, abh1322, doi: [10.1126/science.abh1322](https://doi.org/10.1126/science.abh1322)

—. 2023b, ApJ, 948, 93, doi: [10.3847/1538-4357/ac4ccb](https://doi.org/10.3847/1538-4357/ac4ccb)

Kennicutt, Robert C., J. 1998, ARA&A, 36, 189, doi: [10.1146/annurev.astro.36.1.189](https://doi.org/10.1146/annurev.astro.36.1.189)

Kewley, L. J., Groves, B., Kauffmann, G., & Heckman, T. 2006, MNRAS, 372, 961, doi: [10.1111/j.1365-2966.2006.10859.x](https://doi.org/10.1111/j.1365-2966.2006.10859.x)

Koekemoer, A. M., Faber, S. M., Ferguson, H. C., et al. 2011, ApJS, 197, 36, doi: [10.1088/0067-0049/197/2/36](https://doi.org/10.1088/0067-0049/197/2/36)

Kriek, M., van Dokkum, P. G., Labb  , I., et al. 2009, ApJ, 700, 221, doi: [10.1088/0004-637X/700/1/221](https://doi.org/10.1088/0004-637X/700/1/221)

Larson, R. L., Hutchison, T. A., Bagley, M., et al. 2022, arXiv e-prints, arXiv:2211.10035, <https://arxiv.org/abs/2211.10035>

Leja, J., Carnall, A. C., Johnson, B. D., Conroy, C., & Speagle, J. S. 2019a, ApJ, 876, 3, doi: [10.3847/1538-4357/ab133c](https://doi.org/10.3847/1538-4357/ab133c)

Leja, J., Johnson, B. D., Conroy, C., et al. 2019b, ApJ, 877, 140, doi: [10.3847/1538-4357/ab1d5a](https://doi.org/10.3847/1538-4357/ab1d5a)

Li, W., Nair, P., Rowlands, K., et al. 2023, MNRAS, 523, 720, doi: [10.1093/mnras/stad1473](https://doi.org/10.1093/mnras/stad1473)

Liu, Y., Oguri, M., & Cao, S. 2023, arXiv e-prints, arXiv:2307.14833, doi: [10.48550/arXiv.2307.14833](https://doi.org/10.48550/arXiv.2307.14833)

Lotz, J. M., Koekemoer, A., Coe, D., et al. 2017, ApJ, 837, 97, doi: [10.3847/1538-4357/837/1/97](https://doi.org/10.3847/1538-4357/837/1/97)

Merlin, E., Pilo, S., Fontana, A., et al. 2019, A&A, 622, A169, doi: [10.1051/0004-6361/201833991](https://doi.org/10.1051/0004-6361/201833991)

Merlin, E., Bonchi, A., Paris, D., et al. 2022, ApJL, 938, L14, doi: [10.3847/2041-8213/ac8f93](https://doi.org/10.3847/2041-8213/ac8f93)

Mingozzi, M., James, B. L., Berg, D., et al. 2023, arXiv e-prints, arXiv:2306.15062, doi: [10.48550/arXiv.2306.15062](https://doi.org/10.48550/arXiv.2306.15062)

Neistein, E., van den Bosch, F. C., & Dekel, A. 2006, MNRAS, 372, 933, doi: [10.1111/j.1365-2966.2006.10918.x](https://doi.org/10.1111/j.1365-2966.2006.10918.x)

Oser, L., Ostriker, J. P., Naab, T., Johansson, P. H., & Burkert, A. 2010, ApJ, 725, 2312, doi: [10.1088/0004-637X/725/2/2312](https://doi.org/10.1088/0004-637X/725/2/2312)

Paris, D., Merlin, E., Fontana, A., et al. 2023, arXiv e-prints, arXiv:2301.02179, doi: [10.48550/arXiv.2301.02179](https://doi.org/10.48550/arXiv.2301.02179)

Pascale, M., Frye, B. L., Dai, L., et al. 2022, ApJ, 932, 85, doi: [10.3847/1538-4357/ac6ce9](https://doi.org/10.3847/1538-4357/ac6ce9)

Perrin, M. D., Long, J., Sivaramakrishnan, A., et al. 2015, WebbPSF: James Webb Space Telescope PSF Simulation Tool, Astrophysics Source Code Library, record ascl:1504.007. <http://ascl.net/1504.007>

Planck Collaboration, Ade, P. A. R., Aghanim, N., et al. 2016, A&A, 594, A27, doi: [10.1051/0004-6361/201525823](https://doi.org/10.1051/0004-6361/201525823)

Planck Collaboration, Aghanim, N., Akrami, Y., et al. 2020a, A&A, 641, A12, doi: [10.1051/0004-6361/201833885](https://doi.org/10.1051/0004-6361/201833885)

—. 2020b, A&A, 641, A6, doi: [10.1051/0004-6361/201833910](https://doi.org/10.1051/0004-6361/201833910)

Polletta, M., Dole, H., Martinache, C., et al. 2022, A&A, 662, A85, doi: [10.1051/0004-6361/202142255](https://doi.org/10.1051/0004-6361/202142255)

Polletta, M., Nonino, M., Frye, B., et al. 2023, A&A, 675, L4, doi: [10.1051/0004-6361/202346964](https://doi.org/10.1051/0004-6361/202346964)

Rabien, S., Angel, J., Barl, L., et al. 2019, Astronomy and Astrophysics, 621, doi: [10.1051/0004-6361/201833716](https://doi.org/10.1051/0004-6361/201833716)

Reddy, N. A., Shapley, A. E., Sanders, R. L., et al. 2018, ApJ, 869, 92, doi: [10.3847/1538-4357/aaed1e](https://doi.org/10.3847/1538-4357/aaed1e)

Rennehan, D., Babul, A., Hayward, C. C., et al. 2020, MNRAS, 493, 4607, doi: [10.1093/mnras/staa541](https://doi.org/10.1093/mnras/staa541)

Robotham, A. S. G., Davies, L. J. M., Driver, S. P., et al. 2018, MNRAS, 476, 3137, doi: [10.1093/mnras/sty440](https://doi.org/10.1093/mnras/sty440)

Robotham, A. S. G., D'Silva, J. C. J., Windhorst, R. A., et al. 2023, PASP, 135, 085003, doi: [10.1088/1538-3873/acea42](https://doi.org/10.1088/1538-3873/acea42)

Robotham, A. S. G., Tararu, D. S., Tobar, R., Moffett, A., & Driver, S. P. 2017, MNRAS, 466, 1513, doi: [10.1093/mnras/stw3039](https://doi.org/10.1093/mnras/stw3039)

Rodney, S. A., Riess, A. G., Strolger, L.-G., et al. 2014, AJ, 148, 13, doi: [10.1088/0004-6256/148/1/13](https://doi.org/10.1088/0004-6256/148/1/13)

Rumbaugh, N., Lemaux, B. C., Tomczak, A. R., et al. 2018, MNRAS, 478, 1403, doi: [10.1093/mnras/sty1181](https://doi.org/10.1093/mnras/sty1181)

Sanders, R. L., Shapley, A. E., Jones, T., et al. 2021, ApJ, 914, 19, doi: [10.3847/1538-4357/abf4c1](https://doi.org/10.3847/1538-4357/abf4c1)

Sawicki, M. 2002, AJ, 124, 3050, doi: [10.1086/344682](https://doi.org/10.1086/344682)

Schreiber, C., Glazebrook, K., Nanayakkara, T., et al. 2018, A&A, 618, A85, doi: [10.1051/0004-6361/201833070](https://doi.org/10.1051/0004-6361/201833070)

Scudder, J. M., Ellison, S. L., Torrey, P., Patton, D. R., & Mendel, J. T. 2012, MNRAS, 426, 549, doi: [10.1111/j.1365-2966.2012.21749.x](https://doi.org/10.1111/j.1365-2966.2012.21749.x)

Sengupta, A., Keel, W. C., Morrison, G., et al. 2022, ApJS, 258, 32, doi: [10.3847/1538-4365/ac3761](https://doi.org/10.3847/1538-4365/ac3761)

Shapley, A. E., Sanders, R. L., Salim, S., et al. 2022, ApJ, 926, 145, doi: [10.3847/1538-4357/ac4742](https://doi.org/10.3847/1538-4357/ac4742)

Venkatesan, T. C. A., Batuski, D. J., Hanisch, R. J., & Burns, J. O. 1994, ApJ, 436, 67, doi: [10.1086/174881](https://doi.org/10.1086/174881)

Wang, E., & Lilly, S. J. 2020, ApJ, 892, 87, doi: [10.3847/1538-4357/ab7b7d](https://doi.org/10.3847/1538-4357/ab7b7d)

Weibel, A., Wang, E., & Lilly, S. J. 2023, ApJ, 950, 102, doi: [10.3847/1538-4357/acccfc](https://doi.org/10.3847/1538-4357/acccfc)

Whitaker, K. E., Pope, A., Cybulska, R., et al. 2017, ApJ, 850, 208, doi: [10.3847/1538-4357/aa94ce](https://doi.org/10.3847/1538-4357/aa94ce)

Windhorst, R. A., Cohen, S. H., Jansen, R. A., et al. 2023, AJ, 165, 13, doi: [10.3847/1538-3881/aca163](https://doi.org/10.3847/1538-3881/aca163)

Young, D. R., Smartt, S. J., Mattila, S., et al. 2008, A&A, 489, 359, doi: [10.1051/0004-6361:20078662](https://doi.org/10.1051/0004-6361:20078662)

Zitrin, A., Labb  , I., Belli, S., et al. 2015, ApJL, 810, L12, doi: [10.1088/2041-8205/810/1/L12](https://doi.org/10.1088/2041-8205/810/1/L12)

APPENDIX

Table A1 lists the G165 arc systems used in the Section 4 lens model. The image-system designations for numbers 1–11 follow Frye et al. (2019) with the exception of renaming Arc 1a to be the northernmost image and renaming Arc 1b/c to be the southern images. Ten image systems are new to this study. The table columns are: ID, Right Ascension, Declination, observed AB magnitude (SEXTRACTOR MAG_AUTO) in the F200W filter, spectroscopic redshift (z_{sp}), photometric redshift (z_{ph}), lens-model predicted redshift (z_{mod}), and the arc’s discovery citation. Positions are J2000 on the GAIA DR3 system.

Table A1. Strong-Lensing Image Systems

ID	R.A.	Decl.	$m_{\text{F200W,obs}}$	z_{sp}	z_{ph}	z_{mod}	Ref. ^a
1a	11:27:13.91	+42:28:35.40	24.90	2.2355 ± 0.0003^b	C18, F19
1.1b	11:27:14.70	+42:28:23.81	22.18	2.2357^{cd}			C15, H16
1.1c	11:27:14.80	+42:28:21.23	21.83	2.2357^{cd}			C15, H16
1.2b	11:27:14.74	+42:28:23.17	...	2.2357^{cd}			C15, H16
1.2c	11:27:14.78	+42:28:22.12	...	2.2357^{cd}			C15, H16
2a	11:27:15.34	+42:28:41.05	20.30	1.7833 ± 0.0010^{be}			C18, F19
SNa	11:27:15.31	+42:28:41.02	...	<i>f</i>	<i>g</i>		This study
2b	11:27:15.60	+42:28:34.19	19.89	1.783 ± 0.002^e			C18, F19
SNb	11:27:15.60	+42:28:33.73	...	<i>f</i>	<i>g</i>		This study
2c	11:27:15.98	+42:28:28.72	20.26	1.7834 ± 0.0005^b			C18, F19
SNc	11:27:15.94	+42:28:28.90	...	<i>f</i>	<i>g</i>		This study
3.1a	11:27:14.19	+42:28:32.15			2.21		C18, F19
3.1b	11:27:14.24	+42:28:31.46	22.32		2.2		C18, F19
3.1c	11:27:14.97	+42:28:17.37					C18, F19
3.2a	11:27:14.11	+42:28:32.63					C18, F19
3.2b	11:27:14.36	+42:28:29.62					C18, F19
4a	11:27:14.07	+42:28:32.66	22.96		2.25	2.173	C18, F19
4b	11:27:14.37	+42:28:29.06	22.77				C18, F19
4c	11:27:14.92	+42:28:17.29	23.62				C18, F19
5.1a	11:27:13.20	+42:28:25.73	25.36	3.9530 ± 0.0004^b			F19
5.1b	11:27:13.20	+42:28:24.62	24.88				F19
5.1c	11:27:14.27	+42:28:08.83	26.14				F19
6a	11:27:13.94	+42:28:32.75	24.62		2.18	2.215	C18, F19
6b	11:27:14.36	+42:28:27.64	24.32				C18, F19
6c	11:27:14.84	+42:28:16.84	24.89				C18, F19
7a	11:27:15.24	+42:28:39.46	26.47		2.45	1.859	F19
7b	11:27:15.48	+42:28:33.71	24.13				F19
7c	11:27:15.83	+42:28:28.33	24.23				F19
8.1a	11:27:15.27	+42:28:40.93	24.96 ^h				C18, F19
8.1b	11:27:15.61	+42:28:33.04	22.99 ^h				C18, F19
8.1c	11:27:15.87	+42:28:29.17	24.83 ^h				C18, F19
8.2a	11:27:15.28	+42:28:40.66	24.96 ^h				C18, F19
8.2b	11:27:15.58	+42:28:33.50	22.99 ^h				C18, F19
8.2c	11:27:15.89	+42:28:28.84	24.83 ^h	1.7839 ± 0.0002^b			C18, F19
9a	11:27:15.43	+42:28:40.57	25.54				C18, F19
9b	11:27:15.57	+42:28:36.02	25.33				C18 F19

Table A1 *continued*

Table A1 (*continued*)

ID	R.A.	Decl.	$m_{\text{F200W,obs}}$	z_{sp}	z_{ph}	z_{mod}	Ref. ^a
9c	11:27:16.11	+42:28:28.01	26.10	1.7816 ± 0.0002^b			C18, F19
10a	11:27:15.18	+42:28:38.89	25.93		1.7	1.735	F19
10b	11:27:15.46	+42:28:32.86	25.78				F19
10c	11:27:15.74	+42:28:28.51	25.02				F19
11.1a	11:27:15.77	+42:28:41.92	23.39			2.46	C18, F19
11.1b	11:27:15.79	+42:28:40.78	23.59				C18, F19
11.1c	11:27:16.74	+42:28:22.85	25.21 ^h				C18, F19
12a	11:27:14.52	42:28:23.48	27.61			2.581	This study
12b	11:27:14.73	42:28:17.12	26.27			2.95	This study
13.1a	11:27:14.04	42:28:37.76	26.86			4.209	This study
13.2a	11:27:14.07	42:28:37.37	28.52				This study
13.1b	11:27:14.75	42:28:27.59	27.89				This study
13.2b	11:27:14.71	42:28:28.21	28.68				This study
13.1c	11:27:15.14	42:28:18.82	28.89				This study
13.2c	11:27:15.16	42:28:18.38	28.80				This study
14.1a	11:27:13.09	42:28:26.83	24.62 ^h		2.25	2.342	This study
14.1b	11:27:13.20	42:28:18.77	25.16				This study
14.1c	11:27:13.84	42:28:11.32	24.69 ^h				This study
14.2a	11:27:13.09	42:28:26.94	24.62 ^h				This study
14.2b	11:27:13.21	42:28:18.51	24.21				This study
14.2c	11:27:13.84	42:28:11.32	24.69 ^h				This study
15a	11:27:14.11	42:28:34.10	26.38			2.339	This study
15b	11:27:14.55	42:28:28.27	25.3		2.26		This study
15c	11:27:14.96	42:28:19.09	26.75				This study
16a	11:27:13.47	42:28:27.77	24.41		1.6	1.448	This study
16b	11:27:13.97	42:28:23.90	25.20				This study
16c	11:27:13.46	42:28:21.70	21.88				This study
16d	11:27:14.22	42:28:13.49	24.51				This study
17a	11:27:13.23	42:28:28.61	26.92		6	6.03	This study
17b	11:27:13.22	42:28:23.00	26.89				This study
17c	11:27:14.39	42:28:08.12	29.00				This study
18a	11:27:15.35	42:28:37.70	26.27				This study
18b	11:27:15.43	42:28:36.02	26.09				This study
19a	11:27:14.18	42:28:39.44	27.26				This study
19b	11:27:14.88	42:28:28.69	27.05				This study
19c	11:27:15.30	42:28:20.11	27.10				This study

Table A1 *continued*

Table A1 (*continued*)

ID	R.A.	Decl.	$m_{\text{F200W,obs}}$	z_{sp}	z_{ph}	z_{mod}	Ref. ^a
20a	11:27:14.44	42:28:35.63	-				This study
20b	11:27:14.57	42:28:33.55	-				This study
21a	11:27:15.09	42:28:35.37	-				This study
21b	11:27:15.19	42:28:33.31	-				This study

^aThe image system references are: C15 ([Cañameras et al. 2015](#)), H16 ([Harrington et al. 2016](#)), C18 ([Cañameras et al. 2018](#)), F19 ([Frye et al. 2019](#))

^bSpectroscopic redshift for this arc was measured in this study.

^cSpectroscopic redshift for this arc was measured by [Cañameras et al. \(2015\)](#) or [Harrington et al. \(2016\)](#).

^dSpectroscopic redshift was measured at a different position along this arc.

^eSpectroscopic redshift was first measured for this arc by [Polletta et al. \(2023\)](#).

^fThe photometry will be presented elsewhere (Pierel et al. 2023, in prep.).

^gThe spectroscopic redshift is assumed to be the same as that of the SN host galaxy Arc 2. The spectroscopy will be presented by Chen et al. (2023, in prep.).

^hPhotometry is blended with another image of the same system; the blended photometry is reported.